Journal of
Materials Chemistry A

PAPER

View Article Online
View Journal | View Issue

Cite this: *J. Mater. Chem. A*, 2026, **14**, 18975

Understanding the oxygen reduction/evolution reactions (ORR/OER) on bimetallic Pt–Ir electrocatalysts using *in situ* Raman spectroscopy and DFT

Sonja Blaseio,[a] Thies Reetz,[b] Halil İ. Sözen,[bc] Carsten Dosche,[b] Christian Schneemann,[a] Gustav Sievers,[d] Martin Rohloff,[d] Uta Schlickum,[e] Thorsten Klüner[b] and Mehtap Oezaslan*[a]

Bimetallic platinum–iridium electrocatalysts for oxygen reduction/evolution reactions (ORR/OER) are of great interest for unitized regenerative fuel cells. The potential-dependent formation of catalytically active Pt–Ir species and their resulting electronic structure to accelerate both the ORR and OER are still unknown. Raman spectroscopy is used to monitor *in situ* the potential-resolved electronic and structural interactions of Pt and Ir in sputtered Pt–Ir thin films as model catalyst systems for the ORR and OER. The low coverage of oxygen-based intermediates on the Pt surface sites for Pt–Ir films correlates with enhanced ORR activity. At potentials before and during the OER, further electrochemical oxidation of the Pt–Ir thin films occurs that clearly differs from that of the monometallic films. DFT calculations indicate the formation of hydrous PtO_6–IrO_6 edge-sharing chains with μ-oxo bond linkages to couple Pt and Ir centers electronically. The theoretical stretching and bending motions of these Pt–O–Ir bonds are the most intense vibrations at 494, 542 and 682 cm^{-1} and are in very good agreement with the experimental data (~510, ~540 and 657 cm^{-1}). Very remarkably, theoretical and experimental data uncover a clear shift to lower energy by ~38 cm^{-1} for symmetric stretching of Ir–O–Pt (657 cm^{-1}) compared to Ir–O–Ir (695 cm^{-1}) under OER conditions. In other words, this change in bond strength can be correlated with lower OER activity and indicates a weakening of the Ir–O–Pt bond by ~ 0.48 kJ mol^{-1} compared to IrO_x. Overall, our comprehensive *in situ* Raman and DFT investigations provide new mechanistic insights into the potential-resolved formation of catalytically active Pt–Ir sites for both the ORR and OER.

Received 27th February 2026
Accepted 19th March 2026

DOI: 10.1039/d6ta01745b

rsc.li/materials-a

1. Introduction

Bifunctional Pt–Ir electrocatalysts are commonly studied for use in unitized regenerative fuel cells (URFCs).[1–5] URFCs are a closed loop system, where electrical energy is stored as O_2 and H_2 gas by water splitting (oxygen evolution reaction, OER, and hydrogen evolution reaction, HER) during charging.[5] During discharging the electrical energy is regenerated by the reverse reaction from the stored H_2 and O_2 gas during the oxygen reduction reaction (ORR) and hydrogen oxidation reaction (HOR).[5] In the URFC, both the electrolyzer (for charging) and fuel cell (for discharging) are combined in one device.[1,5,6] URFCs can be operated in two configurations, the constant-gas (CG) and the constant-electrode (CE) modes.[5,7,8] In the CE mode, the URFC has a fixed anode for the HOR/OER and cathode for the ORR/HER, while the gases are switched between the electrolyzer and fuel cell configuration.[5,7] Due to problems with gas mixing, the CG device is the most commonly used and consists of electrode materials that catalyze the ORR/OER on the one hand and the HOR/HER on the other, allowing fast switching between charging and discharging, as well as avoiding mixing of the gases.[5,7] Commonly, bifunctional platinum–iridium-based catalyst materials are employed, which are able to maintain both the oxygen reduction and oxidation reactions, while also withstanding the demanding conditions that prevail under OER potentials.[1,3,7,9,10]

Initially, electrodes that consisted of basic mixtures of Pt black and Ir black or IrO_2 were investigated, showing improved OER activity, but lower ORR activity compared to monometallic Pt electrodes.[11,12] Several studies on Ir-based decorated Pt

---

[a] *Technical Electrocatalysis Laboratory, Institute of Physical Chemistry, Universität Hamburg, Grindelallee 117, 20146 Hamburg, Germany. E-mail: mehtap.oezaslan@uni-hamburg.de*

[b] *Institute of Chemistry, University of Oldenburg, Carl-von-Ossietzky-Str. 9-11, 26129 Oldenburg, Germany*

[c] *Mercedes-Benz Turk A.S., Orhan Gazi Mahallesi, Mercedes Bulvari No. 17/1, Esenyurt, Istanbul 34519, Turkey*

[d] *Elementarhy GmbH, Gustav-Adolf-Straße 78, 22043 Hamburg, Germany*

[e] *Laboratory for Emerging Nanometrology, Institute of Applied Physics, Technische Universität Braunschweig, 38106 Braunschweig, Germany*

nanoparticles (NPs) or Pt layers show the same behavior, namely an enhanced OER activity with increased Ir content and an opposite trend for the ORR.[10,13] Deposition of platinum on iridium or iridium oxide shows a slightly different behavior, whereby, for example, an irreversible formation of hydrous IrO_x increases the ORR activity and stabilizes the platinum on the electrode.[14] On the other hand, Pt deposited on IrO_2 exhibits higher ORR activity compared to Pt particles deposited on hydrous IrO_x.[15] To improve the homogeneous distribution of Ir in the catalyst layer, Pt–Ir alloys have been prepared and investigated for the ORR/OER bifunctionality. Du *et al.* observed a decrease in ORR activity with increased Ir content in the alloy and an opposite trend for the OER, similar to physically mixed Pt and Ir material systems.[1] However, the OER activity is always lower compared to monometallic iridium oxide catalysts.[1] In contrast, for all Ir concentrations of Pt–Ir alloy NPs, an increase in OER performance compared to monometallic Ir was found.[16] Additionally, the study indicates that surface alloying effects of Pt and Ir change the rate determining step for the OER from the adsorption of hydroxyl groups to the dissociation of water, which is explained by a partial electron transfer from iridium to platinum.[16] Similarly, the ORR activity of Pt–Ir alloy NPs increases with 5–20% iridium in the alloy.[12] At higher Ir concentrations, the activity decreases again, due to the influence of Ir–OH surface groups on neighboring Pt atoms.[12] The resulting interatomic charge transfer from platinum to iridium is evaluated by XPS.[12] This discrepancy in the various Pt–Ir nanomaterial systems clearly shows that the interactions between both metals for the ORR and OER are not yet fully understood to date.

Furthermore, the metallic state for both components is not stable and Pt and Ir (surface) oxides are formed under these harsh conditions.[17–19] Experimentally, the oxidation mechanism of single crystalline Ir(111) has been studied by surface X-ray diffraction (XRD).[20] First, a hexagonal trilayer of O–Ir–O forms, followed by a phase transition to a multilayered oxide with a corundum Ir_2O_3 structure as an intermediate and then changes to the thermodynamically stable bulk rutile IrO_2.[20] The initial formation of the O–Ir–O trilayer has been confirmed by DFT calculations.[21] However, under OER relevant potentials XPS and atomic force microscopy (AFM) indicate the evolution of similarly roughened/buckled surface oxides containing mostly Ir^{4+} species, independent of the initial iridium surface orientation and oxidation state (single crystal or IrO_2).[17] Pavlovic *et al.* extensively investigated amorphous IrO_x during the OER in alkaline and acidic media using *in situ* Raman spectroscopy.[22,23] For IrO_x deposited on Ir or Au foil, exposure to an aqueous electrolyte leads to hydrated IrO_x in the form of polymeric edge sharing IrO_6 octahedra, that are connected *via* μ-oxo type bridges.[22,23] These polymeric IrO_6 chains have a flexible ligand environment, which facilitates the exchange of oxygen atoms during the OER.[22,23] The formation of this structure manifests in a broad range of Raman bands observed between 300 and 800 cm^{-1} for IrO_x, which were also confirmed by Zhao *et al.*[24]

The oxidation of platinum commences differently than that of iridium. Scanning tunnelling microscopy (STM) shows the formation of Pt oxide chains that buckle out of the surface plane, forming Y shaped branched structures on a Pt(111) surface.[25] These findings were confirmed by DFT calculations[21,26] and further suggest that a transition to a 2D PtO_2 film occurs as the oxidation of the surface progresses. *In situ* Raman spectroscopy investigations on single crystalline Pt(111) and Pt(100) indicate the evolution of (su)peroxo-like 2D platinum surface oxides between 1.0 and 1.2 V_{RHE}.[27] Above 1.3 V_{RHE}, the separate formation of an amorphous hydrous α-PtO_2 3D oxide commences independently, with a broad Raman band at around 500–590 cm^{-1}, that could not be resolved further.[27] However, the oxidation of bimetallic Pt–Ir surfaces has only been investigated by DFT calculations so far. For example, alloying Pt with Ir shows a positive ΔG of mixing.[28] At anodic potentials, these repulsive interactions push platinum out of the alloy and facilitate the separate oxide formation (PtO_2 and IrO_2).[28] These findings are in agreement with DFT calculations by Wittemann *et al.* showing that thermodynamically rutile IrO_2 is the most stable on bimetallic PtIr(111) and $Pt_3Ir(111)$, while α-PtO_2 is only metastable.[21]

To gain insights into the formation of oxide species on bimetallic Pt–Ir surfaces under potentials relevant for the ORR and OER, Pt–Ir thin films were investigated by *in situ* Raman spectroscopy and DFT. Pt–Ir thin films with atomic Pt : Ir ratios of 1 : 1 and 3 : 1 were chosen as model systems for studying surface changes of mixed Pt and Ir oxides evolving during the ORR and OER. The origin of the lower OER activity of these bimetallic films could be uncovered and is based on the significant weakening of the Pt–O–Ir bond strength compared to Ir–O–Ir.

2. Experimental

2.1. Chemicals

For thin film deposition, iridium (MaTeck, 99.95%) and platinum (MaTeck, 99.95%) targets were used. All *in situ* Raman spectro-electrochemical experiments were performed in 0.1 M $HClO_4$ prepared from concentrated $HClO_4$ (Sigma Aldrich, 70 vol%, 99.999%) and ultra-pure water (18.18 MΩ cm at 25 °C).

2.2. Thin film preparation

Bimetallic and monometallic thin films were deposited without heating using two magnetrons with planar targets of Ir and Pt by physical vapor deposition (PVD) in a Leybold Univex 300 instrument. The layers of bimetallic films were deposited with atomic Pt : Ir ratios of 1 : 1 and 3 : 1 using alternating sputtering onto a gas diffusion layer (GDL, Freudenberg, H23C6), as described previously by Sievers *et al.*[29,30] The alternating process was repeated 50 times, and iridium was always the last step, resulting in a total metal loading of 0.4 $mg_{metal}\ cm_{geo}^{-2}$.

2.3. *In situ* electrochemical Raman spectroscopy measurements

Electrochemical measurements were conducted in a three-electrode custom-made spectro-electrochemical cell (Fig. S1 of the SI) using a potentiostat (Gamry, Reference 600). In a three electrode-arrangement, sputtered Pt–Ir thin films on the GDL

(Freudenberg, H23C6), gold mesh and mercury–mercury sulfate electrode (ALS-Japan, RE-2CP) were used as the working, counter and reference electrodes, respectively. A chronoamperometric method was used by increasing the potential in 100 mV steps from 0.3 V_{RHE} to 1.6 V_{RHE} in 0.1 M $HClO_4$. All reported potentials were corrected for the iR-drop.

In situ Raman spectra of the Pt–Ir thin films were acquired using a Witec alpha300 RSA confocal microscope with an excitation wavelength of 785 nm, a laser power of 2 mW, 300 lines mm^{-1} grating and Zeiss W Plan-Apochromat 63×/1.0 NA objective. At each potential, Raman spectra were recorded with 5 s acquisition time and averaged over 50 exposures. *Ex situ* Raman spectra were recorded with a Zeiss EC Epiplan-Neofluar Dic 50×/0.8 NA objective using 1 mW laser power. All Raman spectra were background subtracted and smoothed by Savitsky–Golay filtering over a window size of 32 points using the software Project SIX (WITec, version 6.1).

2.4. *Ex situ* characterization

The structure and morphology of Pt–Ir thin films were evaluated by using a Helios G4 CX scanning electron microscope (SEM) equipped with an Everhart–Thornley secondary electron detector. An accelerating voltage of 5 kV and a current of 100 pA were applied. The SEM images were acquired at a working distance of 4.1 mm.

X-ray diffraction (XRD) data of sputtered Pt–Ir thin films were measured using a 2-theta-diffractometer (Bruker, D2Phaser) equipped with a Cu Kα X-ray source (wavelength of 1.54 Å) and a position-sensitive detector (SSD160 1D-Detector) in Bragg–Brentano geometry. The operating voltage and current were 30 kV and 10 mA, respectively. The measurement parameters used were as follows: 2θ range from 10 to 95°, step size of 0.01°, holding time of 7 s per step, divergence slit of 1 mm, secondary soller slit of 2.5° and sample rotation of 20 rpm. The XRD profiles were analyzed with the software TOPAS (Bruker, version 5). The quantitative Rietveld refinement analysis was conducted with the following fit parameters: background coefficients, displacement correction, peak shapes and cell parameters. The quality of the fit was evaluated with the R-weighted pattern (Rwp).

To determine the bulk atomic Pt : Ir ratios of the thin films, a micro-X-ray fluorescence (μ-XRF) spectrometer (Bruker, M4 Tornado plus) equipped with a rhodium X-ray source, operated at 50 kV and 300 μA, a 20 μm poly-capillary and two SDD detectors (type: 660 PAR -LE) was employed. Pt and Ir Lα characteristic lines from three randomly distributed point measurements with a spot size of 20 μm and acquisition time of 60 s were analyzed using the software M4 TORNADO (Bruker, version 1.6.621.0).

For X-ray photoelectron spectroscopy (XPS) measurements, an ESCALAB 250 Xi instrument (Thermo Fisher) equipped with an Al source (1486.6 eV Kα) was employed. The spot size used was 650 μm and no charge compensation was carried out. The acquisition parameters of Pt 4f, Ir 4f, O 1s and C 1s XPS spectra are listed in Table S1. The spectra were analyzed using the software Avantage v5.9952. For background correction, a combined model of Shirley and polynomial was applied, while the XPS signals were fitted with mixed Lorentzian–Gaussian functions with optional asymmetric and tailing functions for any metal components. The binding energies of the deconvoluted XPS spectra were referenced to the C 1s peak of the aliphatic hydrocarbon component at 284.8 eV.

2.5. Electrochemical characterization of Pt–Ir thin films using an impinging jet flow cell

Electrochemical measurements were conducted in a custom-made impinging jet flow cell setup[31] equipped with a potentiostat (Biologic, VSP-300) and a syringe pump (KD Scientific, Legato 210). The three-electrode arrangement consisted of Pt–Ir thin films as the working electrode, gold mesh as the counter electrode and the mercury–mercury sulfate reference electrode (ALS-Japan, RE-2CP). The reference electrode was calibrated against a reversible hydrogen electrode using a poly-Pt electrode in H_2-saturated 0.1 M $HClO_4$. The Pt–Ir thin films were glued onto a polished glassy carbon (GC) substrate using a conductive colloidal gold paste (Plano GmbH, #16022). All potentials are referred to the reversible hydrogen electrode (RHE) and were corrected for the iR-drop. In a pre-conditioning step, all catalysts were electrochemically treated by 100 potential cycles between 0.05 V_{RHE} and 1.40 V_{RHE} at a scan rate of 100 mV s^{-1} in argon-saturated 0.1 M $HClO_4$. Afterwards, five cyclic voltammetry (CV) profiles were recorded between 0.05 and 1.40 V_{RHE} at 50 mV s^{-1} to determine the electrochemically active surface area (ECSA) derived from the hydrogen underpotential deposition (H_{UPD}). The H_{UPD} was obtained from integrating the hydrogen ad-/desorption region, correcting it by using the double layer current and assuming pseudo-capacities of 210 μC cm^{-2} for poly-crystalline Pt,[32] 179 μC cm^{-2} for poly-crystalline Ir,[33] 195 μC cm^{-2} for a Pt : Ir ratio of 1 : 1 and 202 μC cm^{-2} for a Pt : Ir ratio of 3 : 1, respectively. In addition, the ORR and OER polarization curves were measured in one linear sweep voltammogram (LSV) from 0.05 to 1.60 V_{RHE} at a scan rate of 1 mV s^{-1} and a flow rate of 1 mL min^{-1} in O_2-saturated 0.1 M $HClO_4$.

2.6. Density functional theory (DFT)

All theoretical calculations were performed with the ORCA software package.[34] The B3LYP hybrid functional was employed for the geometry optimization of the clusters and calculation of Raman spectra.[35] The functional was chosen based on a study by Tekarli *et al.*,[36] showing favorable effects of hybrid functionals on predicted properties of transition metal complexes. In addition, a prior study by Pavlovic *et al.*[22] showed great success of the same functional in similar systems. The geometry optimization convergence threshold was set to 5×10^{-6} E_H for the energy criterion and 10^{-4} E_H/a_0 for the gradient. D3-Grimme dispersion correction with zero damping and ZORA relativistic correction were used and all electrons were modeled explicitly.[37,38] Singlet/doublet states were found to be the most energetically favorable and therefore applied in all calculations. Implicit solvation in water using the Conductor-like Polarizable Continuum Model (CPCM) method was considered. The resulting Raman spectra of the iridium oxo-hydroxy complex (Fig. S2) resembled those without the effects of solvation with water molecules and therefore were not further included in our simulations. Raman spectra were calculated using numerical frequency calculations.

3. Results

3.1. Morphology and structure of the bimetallic Pt–Ir thin films

The bulk composition and structure of Pt–Ir thin films were investigated by SEM, XRD and μ-XRF techniques. The bimetallic Pt–Ir thin films were prepared by alternating magnetron sputtering of Pt and Ir targets for 50 cycles onto a PTFE/carbon-based gas diffusion layer (GDL). Iridium was always the last in the alternating cycle process between both metals. Throughout the paper, sputtered thin films with atomic Pt : Ir ratios of 1 : 1 and 3 : 1 will be referred to as PtIr(1 : 1) and PtIr(3 : 1), respectively. For comparison, monometallic Pt and Ir thin films were prepared by the same technique.

At low magnification, the top view SEM images of the PtIr(1 : 1) and PtIr(3 : 1) thin films (Fig. S3a and S3b) show the typical surface morphology with the so-called "cauliflower" growth. The rough surface forms from the individual grains, as they are deposited onto the GDL during sputtering. Quantitative μ-XRF analysis (Table S2) confirms that the bulk Pt : Ir ratios are in line with the expected values of 1 : 1 (Pt: 47 ± 2 at% and Ir: 53 ± 2 at%) and 3 : 1 (Pt: 75 ± 1 at% and Ir: 25 ± 1 at%).

Furthermore, the crystal phases and crystallite sizes of the sputtered Pt–Ir, Pt and Ir thin films were established by XRD. All XRD profiles with the respective fits obtained from the quantitative Rietveld refinement analysis are displayed in Fig. S3c. The peaks at 2θ values of ∼40°, ∼46°, ∼67°, ∼82° and ∼86° correspond to the lattice planes of (111), (200), (220), (311) and (222) of a face-centered cubic (fcc) disordered Pt, Ir and Pt–Ir alloy unit cell with a space group of $Fm\bar{3}m$. All thin films show broadened peaks, indicating small crystallite sizes. Table S3 summarizes the best fit results of the quantitative Rietveld refinement analysis and the respective alloy composition *via* Vegard's law for the PtIr(1 : 1), PtIr(3 : 1), Pt and Ir thin films. Both bimetallic Pt–Ir thin films contain at least two fcc disordered Pt–Ir alloy crystal phases. The PtIr(1 : 1) thin film consists of a 1 : 1 ratio of the $Pt_{95}Ir_{05}$ alloy phase (mean crystallite size of 6.1 ± 0.2 nm) and $Pt_{40}Ir_{60}$ alloy phase (7.2 ± 0.2 nm), while the 40 wt% $Pt_{52}Ir_{48}$ phase (8.2 ± 0.3 nm) and 60 wt% monometallic Pt (6.0 ± 0.1 nm)

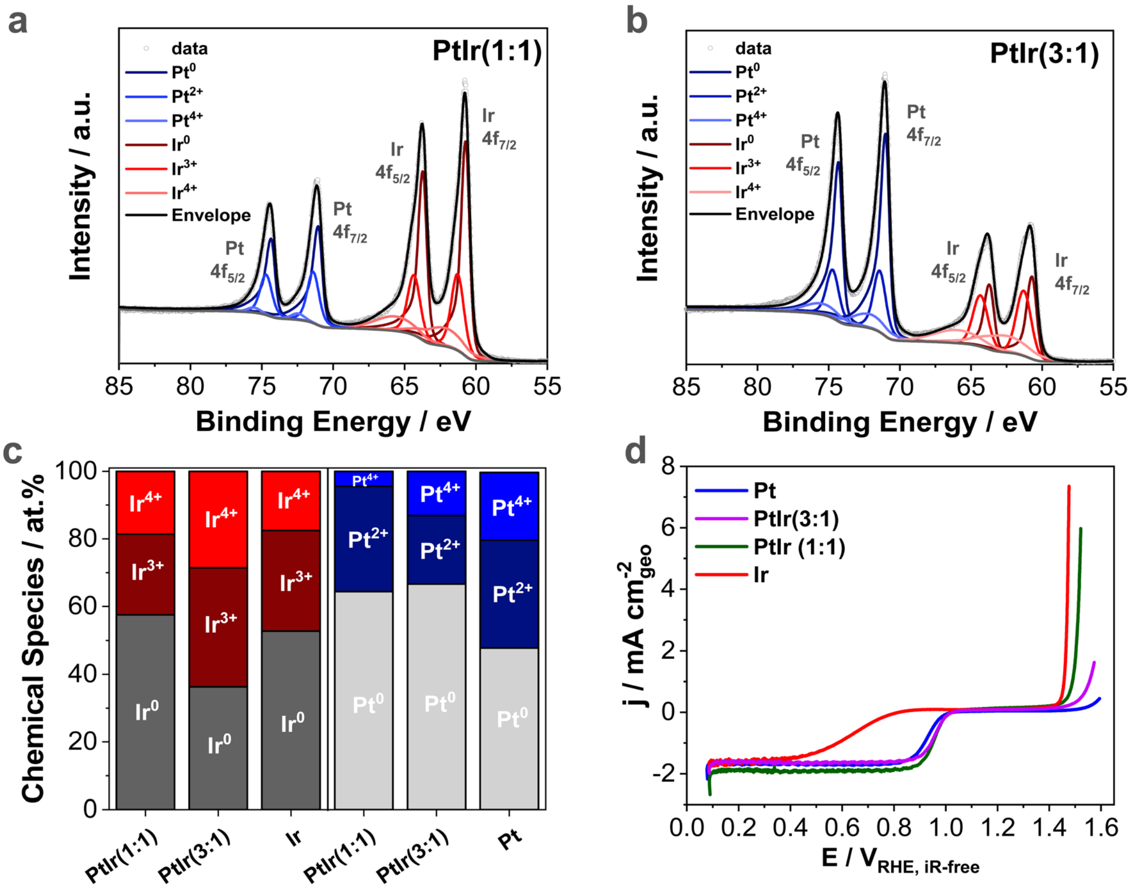

Fig. 1 (a and b) *Ex situ* high-resolution Pt and Ir 4f XPS spectra of the Pt–Ir thin films. Light grey circles represent the measured data, the envelope is shown in black and the background is denoted in grey. Pt^0, Pt^{2+} and Pt^{4+} species are plotted in blue, while Ir^0, Ir^{3+} and Ir^{4+} species are displayed in red. (c) Quantitative surface analysis of the high-resolution Pt and Ir $4f_{7/2}$ XPS spectra to determine each species (Pt^0, Pt^{2+} and Pt^{4+} and Ir^0, Ir^{3+} and Ir^{4+}). High-resolution Pt and Ir 4f XPS spectra of the monometallic Pt and Ir thin films are displayed in Fig. S4. (d) ORR and OER polarization curves of the PtIr(1 : 1) (green), PtIr(3 : 1) (pink), Pt (blue) and Ir (red) thin films with a total loading of 0.4 $mg_{metal}\ cm_{geo}^{-2}$. The polarization curves were recorded in one scan from 0.05 to 1.6 $V_{RHE,\ iR\text{-}free}$ at a scan rate of 1 mV s^{-1} and a flow rate of 1 mL min^{-1} in O_2-saturated 0.1 M $HClO_4$ using an impinging jet flow cell.

are present for the PtIr(3 : 1) thin film. The monometallic Pt and Ir thin films show slightly smaller mean crystallites of 5.1 ± 0.1 nm and 4.5 ± 0.1 nm, respectively.

Surface-sensitive XPS measurements were employed to investigate the surface composition and oxidation state of Pt and Ir species. High-resolution Pt and Ir 4f XPS data of the PtIr(1 : 1) and PtIr(3 : 1) thin films are displayed in Fig. 1a–b, respectively. The deconvolution of the Pt $4f_{7/2}$ XPS spectra clearly implies the presence of three components at binding energies (BEs) of 71.1 eV, 71.4 eV and 72.5 eV, assigned to metallic Pt, Pt^{2+} and Pt^{4+} species, respectively.[39,40] The Ir $4f_{7/2}$ XPS spectra can be deconvoluted into three chemical species at BEs of 60.6 eV, 61.3 eV and 62.2 eV, which are attributed to metallic Ir, Ir^{3+} and Ir^{4+} species, respectively.[39,41] Based on the quantification of the Pt and Ir $4f_{7/2}$ XPS data, the surface Pt : Ir ratio was determined to be 29 : 71 at% for PtIr(1 : 1), while for PtIr(3 : 1) a higher Pt surface content is observed (Pt : Ir ratio of 44 : 56). Obviously, the surface of both thin films is enriched with iridium compared to the bulk, which is very likely related to the preparation of the thin films as the last step in the 50 cycles of sputtering was iridium.

Quantitative XPS analysis of the different oxidation states of Pt and Ir is displayed in Fig. 1c. The surface of the PtIr(1 : 1) thin film contains around 58 at% Ir^0, 24 at% Ir^{3+} and 18 at% Ir^{4+} species. In contrast, for PtIr(3 : 1), the quantification of the Ir $4f_{7/2}$ XPS data reveals a high contribution of the oxidized Ir species (in total 64 at% = 35 at% Ir^{3+} and 29 at% Ir^{4+}) and only 36 at% metallic Ir. For platinum, the metallic contribution of both bimetallic Pt–Ir thin films is comparable (∼65 at%), while around 35 at% are oxidized to Pt^{2+} and Pt^{4+} species. As the samples were stored in air, iridium is more oxidized compared to platinum, due to its higher oxophilic character.[42]

The Ir and Pt 4f XPS data for both monometallic thin films are displayed in Fig. S4. The monometallic Ir thin film shows a similar contribution of the three chemical species (Ir^0, Ir^{3+} and Ir^{4+}) compared to PtIr(1 : 1). For monometallic platinum, this is different. A much higher concentration of oxidized Pt^{2+} and Pt^{4+} species (52 at%) is observed than for both bimetallic Pt–Ir films. This reveals a preferential oxidation of Ir for the bimetallic thin films, while platinum tends to appear more reduced. However, this could have occurred due to the enrichment of iridium or it being sputtered last on the surface, which protects the platinum in the sub-surface from air oxidation.

Overall, *ex situ* characterization highlights the formation of a rough and oxidized surface of the as-prepared Pt–Ir thin films. Based on the bulk XRD analysis, both bimetallic films are composed of one Pt-rich and one fcc disordered Pt–Ir alloy phase with average crystallite sizes between 5 and 8 nm. Surface-sensitive XPS analysis reveals the significant air oxidation of the surfaces of all thin films and their enrichment in iridium oxide surface species.

3.2. Activities of the Pt–Ir, Pt and Ir thin films towards the ORR and OER

To establish the catalytic activity of bimetallic Pt–Ir thin films, polarization curves for the ORR and OER were collected in O_2-saturated 0.1 M $HClO_4$ using an impinging jet flow cell (Fig. 1d).[31] The electrochemically active surface area was determined by the underpotential deposition of hydrogen (H_{UPD}) obtained from the cyclic voltammetry (CV) data between 0.06 and 0.40 V_{RHE}, as shown in Fig. S5. We note that due to the presence of Ir–OH surface coverage, CO stripping experiments would have been a more suitable method to determine the electrochemically active surface area (ECSA).[43–45] Nevertheless, the general trend is still observed from the H_{UPD}-based ECSA.

In Fig. S5, the CV profiles of monometallic and bimetallic thin films show the characteristic features of metallic Pt and Pt–Ir, related to the underpotential hydrogen deposition (H_{UPD}) region (0.06–0.40 V_{RHE}), capacitive double layer region (0.40–0.60 V_{RHE}) and (hydr)oxide formation/reduction above 0.6 V_{RHE}. Only the monometallic Ir thin film shows a strong oxide surface with a redox couple of Ir^{3+}/Ir^{4+} between 0.7 and 1.0 $V_{RHE,iR\text{-}free}$ and a minor H_{UPD} region below 0.3 $V_{RHE,iR\text{-}free}$. In addition, the CV profiles exhibit varying current densities in the capacitive double layer region (0.4–0.6 V_{RHE}), indicating different contributions of sputtered films and the PTFE/carbon-based GDL substrate. More precisely, the capacitive current density for monometallic Pt is the lowest, signifying the formation of a dense bulk metal film due to the continuous dissolution/re-deposition of amorphous Pt species during the pre-conditioning step (100 potential cycles between 0.05 and 1.40 V_{RHE}, Fig. S6). In contrast, the bimetallic and Ir thin films show larger capacitive current density, indicating a less dense metal film with a significant contribution of the GDL substrate exposed to the electrolyte solution.

In Fig. 1d, the polarization curves show the ORR activity for Pt–Ir and Pt films with different extents. Due to the strong oxidation of the Ir surface, no ORR activity is observed. Table S4 sums up the Pt–Ir-based surface area specific ORR activities (SA_{ORR}) determined from the H_{UPD}-based kinetic current at 0.90 $V_{RHE,iR\text{-}free}$. The Koutecký–Levich equation was applied to determine the limiting current density (j_{lim}) and kinetic current density (j_{kin}). Very recently, we have demonstrated that the j_{lim} characteristics measured in our impinging jet flow cell are in very good agreement with the data from computational fluid dynamics (CFD) and our developed universal analytical model.[31] It is noted that the SA_{ORR} decreases in the sequence: PtIr(3 : 1) (88 μA cm_{HUPD}^{-2}) > PtIr(1 : 1) (57 μA cm_{HUPD}^{-2}) > Pt (54 μA cm_{HUPD}^{-2}) >> Ir (3 μA cm_{HUPD}^{-2}), respectively. The observed activity difference can be explained by a 2–3-times higher surface area and larger roughness factor (RF) of the bimetallic thin films compared to monometallic Pt. In other words, the RF values determined by the ratio between H_{UPD} and geometric surface area are 19 for monometallic Pt, 56 for PtIr(1 : 1) and 39 for PtIr(3 : 1).

At 1.50 $V_{RHE,\ iR\text{-}free}$, the monometallic Ir thin film shows the highest SA_{OER} with 245 μA cm^{-2}_{HUPD}. For PtIr(1 : 1), the SA_{OER} is reduced by 7-fold (34 μA cm^{-2}_{HUPD}), while a further increase in platinum content leads to much lower SA_{OER} with 8 μA cm_{HUPD}^{-2}. This value is only slightly higher compared to that for the monometallic Pt thin film (4 μA cm_{HUPD}^{-2}).

Altogether, the Pt–Ir thin films show catalytic activities towards the ORR and OER to different extents, demonstrating their unique bifunctionality for unitized regenerative fuel cells.

3.3. *In situ* Raman spectroscopy of Pt–Ir, Ir and Pt thin films

Surface-sensitive Raman spectroscopy was used to understand the bifunctionality, *in situ* formation of catalytically active Pt–Ir oxide sites and their electronic structure for the ORR and OER between 0.3 and 1.6 V_{RHE} in 0.1 M $HClO_4$. The high roughness factor (RF) and small crystallite sizes derived from the CV and XRD data show the nano-structuring of the sputtered film surface, allowing the *in situ* detection of the sufficient Raman scattering signal of the catalytically active metal oxide species formed during the ORR and OER.

Initially, the PtIr(1 : 1), PtIr(3 : 1), Pt and Ir thin films were investigated *ex situ* and at open circuit potential (OCP), as shown in Fig. S7. From the *ex situ* data, all thin films show broad Raman bands between 400 and 700 cm^{-1}, indicating the presence of disordered amorphous Pt and Ir oxide species. Single crystalline structures of these oxides would exhibit sharp distinct Raman peaks.[46–48] Platinum oxide only forms as an amorphous oxide in all platinum containing thin films, as it does not exhibit any sharp and resolved Raman bands. The Pt–Ir and Ir thin films show two distinct bands at 550 cm^{-1} (E_g) and 704 cm^{-1} (B_{2g}), indicating the formation of some ordered rutile IrO_2 on the surface (peak assignments in Table S5).[46,47] Upon exposure to 0.1 M $HClO_4$ (Fig. S7b), the peak at 704 cm^{-1} immediately disappears, indicating the hydration of the structured rutile IrO_2 to form hydrous IrO_x.[22] Note that the weak band at 933 cm^{-1} is assigned to ClO_4^- of the 0.1 M $HClO_4$ electrolyte solution (Fig. S8).[27,49–51]

To investigate the potential-dependent surface changes and oxide formation for each of the thin films, a chronoamperometric method was applied, where the potential was shifted in 100 mV steps from 0.3 V_{RHE} to 1.6 V_{RHE} in 0.1 M $HClO_4$. Each potential was held for 5 minutes, while Raman spectra were accumulated every 5 s. The detailed evolution of the Raman spectra recorded from all thin films between 0.8 V_{RHE} and 1.6 V_{RHE} are illustrated in Fig. S9. To obtain a fundamental understanding of the oxide formation and its electronic structure on the bimetallic thin films under ORR and OER conditions, the *in situ* Raman spectra of the monometallic Pt and Ir thin films will be described first.

3.3.1 *In situ* Raman spectra of monometallic thin films

Iridium. Potential-resolved *in situ* Raman spectra for the Iridium thin film at low potentials (below 0.8 V_{RHE}) are displayed in Fig. S10. At 0.2 V_{RHE}, the broad peak at around 548 cm^{-1} (already observed at OCP) disappears, and simultaneously a sharp band at 564 cm^{-1} emerges and is retained until 0.6 V_{RHE}. From 0.8 V_{RHE} to higher potentials, where the transition of Ir^{3+} to Ir^{4+} species occurs, a broadening of the Raman bands is visible. At this potential, a second distinct peak at 498 cm^{-1} is observed, while two bands at 295 cm^{-1} and 336 cm^{-1} appear at the same time. In the potential region, where the ORR takes place (0.8 to 1.2 V_{RHE}, Fig. 1d), this broad peak structure between 400 and 700 cm^{-1} remains unchanged, while the band at 564 cm^{-1} shifts to 548 cm^{-1} at 1.0 V_{RHE}. From 1.3 V_{RHE} to further higher potentials, the Raman spectra change significantly (Fig. S9a), indicating additional electrochemical oxidation of the Ir thin film. More precisely, three distinct peaks at 465 cm^{-1}, 498 cm^{-1} and 681 cm^{-1} appear, while the bands at 548 cm^{-1} and 602 cm^{-1} diminish. These spectral features are retained until 1.5 V_{RHE}. Increasing the potential to 1.6 V_{RHE}, the Raman band at 681 cm^{-1} shifts only by 14 cm^{-1} to 695 cm^{-1}, while the rest of the spectrum remains unchanged (Fig. 2a).

Generally, our results for the iridium thin film between 0.8 and 1.6 V_{RHE} are in good agreement with the formation of hydrous IrO_x species proposed by Pavlovic *et al.*[24] and Zhao *et al.*[24] For instance, the sharp Raman band at 564 cm^{-1} observed below 0.8 V_{RHE} was previously reported for IrO_2 in several studies in acidic[52,53] and alkaline[23] environments. In all studies, this peak was attributed to highly stable Ir^{3+}–OH species. At 0.8 V_{RHE}, a second band at 498 cm^{-1} and a general broadening of the sharp band occur, similar to the IrO_2 study reported by Zou *et al.*[52] This additional Raman band is assigned to the Ir–O stretching frequency and is associated with the formation of Ir^{4+} centers.[22,24] It suggests that the transition of Ir^{3+} to Ir^{4+} species already takes place starting from 0.8 V_{RHE}. A shoulder at 602 cm^{-1} appears, which is related to an Ir^{3+}–O–Ir^{4+} stretching frequency and gets more pronounced, when the potential is increased further.[22]

At 1.0 V_{RHE}, the peak at 564 cm^{-1} shifts to a higher energy at 548 cm^{-1}, which could indicate either the formation of some rutile-type IrO_2 or the association with Ir^{3+} centers.[22,24] In addition, a new band at 465 cm^{-1} is formed that is discussed in the literature to be associated with adsorbed perchlorate anions on the IrO_x surface.[51] Two Ir^{4+}–O bending vibrations simultaneously appear at 295 cm^{-1} and 336 cm^{-1}. The schematic of the bending and stretching motions are shown in Fig. S11. This arrangement of the Raman peaks remains during the entire ORR potential range (from 0.8 to 1.2 V_{RHE}).

The assignments of the Raman bands detected at 1.2 V_{RHE} and 1.6 V_{RHE} are summarized in Table 1 and are mainly based on the oxidation of anodically deposited IrO_x films for the OER reported by Pavlovic *et al.*[22] and Zhao *et al.*[24] We chose these potentials due to the observed significant changes in the potential-induced Raman spectra, which are correlated with the formation of catalytically active species during the ORR (<1.23 V_{RHE}) and OER (~1.6 V_{RHE}).

At 1.3 V_{RHE}, the oxidation of the remaining Ir^{3+} to Ir^{4+} centers continues, as evidenced by the disappearance of the Raman band associated with the Ir^{3+} center at 602 cm^{-1} and the presence of two strong bands at 498 cm^{-1} and 681 cm^{-1}. Both bands are related to Ir–O stretching frequencies with only Ir^{4+} centers.[22] Up to 1.5 V_{RHE}, the peak positions remain unchanged, indicating the stability of the octahedral IrO_x lattice with Ir–O. At a potential of 1.6 V_{RHE}, the band at 681 cm^{-1} slightly shifts to a higher energy at 695 cm^{-1}, signifying the gradual oxidation of some Ir^{4+} to Ir^{5+} centers. According to the DFT calculations, a blue shift in the predicted Raman spectrum is either due to the presence of the Ir^{4+}-Ir^{5+}-Ir^{4+} trimer compared to the Ir^{4+}-Ir^{4+}-Ir^{4+} trimer or associated with a shortening/strengthening of the Ir–O bond length.[22,54]

Overall, various Raman bands present at around 550 cm^{-1} are related to a mixture of Ir^{3+}/Ir^{4+} species within a hydrated IrO_x structure in the potential range of the ORR. With increasing the potential until the OER sets in, all Raman bands

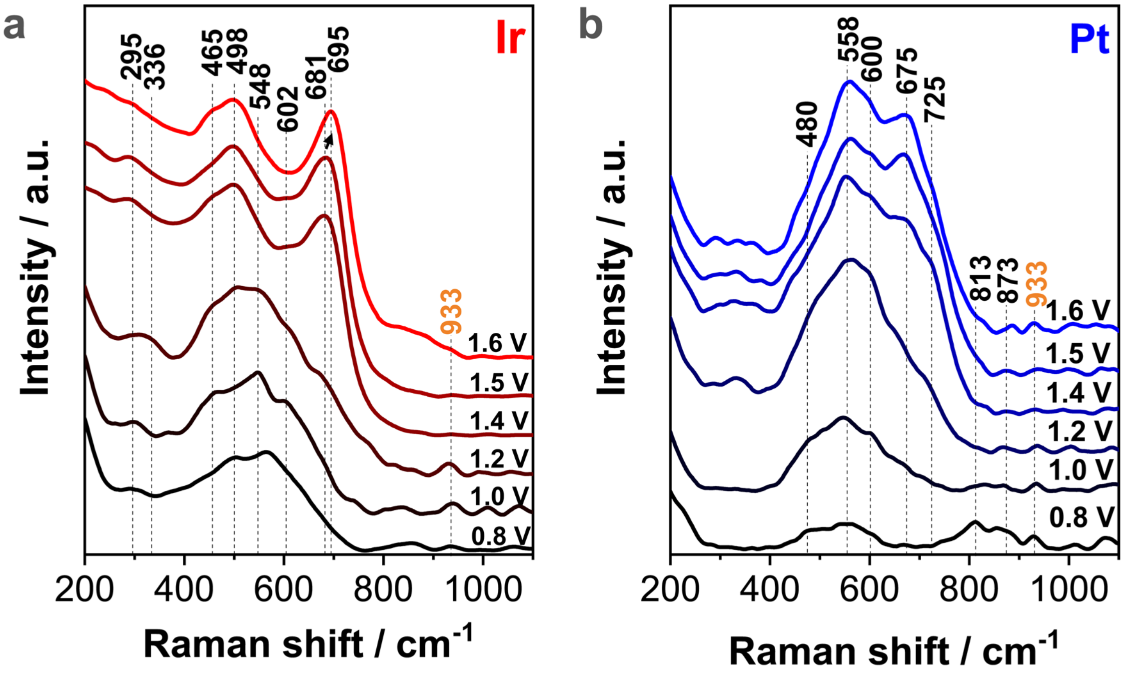

Fig. 2 *In situ* Raman spectra of (a) monometallic Ir and (b) monometallic Pt thin films in the potential range of 0.8–1.6 V_{RHE} in 0.1 M $HClO_4$. Peak assignments of the respective Raman data at 1.2 and 1.6 V_{RHE} are shown in Tables 1 and 2. The position at 933 cm^{-1} is ascribed to the adsorbed ClO_4^- anion.

Table 1 Raman peaks and corresponding mode of vibration of the iridium thin film by applying a potential of 1.2 V_{RHE} and 1.6 V_{RHE} in 0.1 M $HClO_4$. Assignments are based on the works reported by Pavlovic *et al.*[22] and Zhao *et al.*[24]

Potential	Raman shift/cm^{-1}	Mode of vibration
1.2 V_{RHE}	295	Ir^{4+}–O–Ir^{4+} bend
	336	Ir^{4+}–O–Ir^{4+} bend
	465	$ClO_{4(ads)}^-$
	498	Ir^{4+}–O–Ir^{4+} stretch
	548	Rutile IrO_2 (E_g)
	602	Ir^{3+}–O–Ir^{4+} stretch
	681 (very weak)	Ir^{4+}–O–Ir^{4+} stretch
1.6 V_{RHE}	465	$ClO_{4(ads)}^-$
	498	Ir^{4+}–O–Ir^{4+} stretch
	695	Ir^{4+}–O–Ir^{5+} stretch

corresponding to Ir^{3+} centers diminish, and simultaneously the formation of Ir^{4+} centers are observed by two strong bands at 498 cm^{-1} and 695 cm^{-1}.

Platinum. The *in situ* Raman spectra from the monometallic Pt thin film between 0.3 and 0.8 V_{RHE} are displayed in Fig. S12. Evidently, more Raman peaks are observed at these potentials compared to the monometallic Ir film. Especially in the region between 700 and 1000 cm^{-1}, several strong bands are visible and change their Raman frequency with the applied potential. At 0.4 V_{RHE}, several bands between 400 and 600 cm^{-1} appear simultaneously and become more pronounced, as the potential is increased to 0.8 V_{RHE}. The *in situ* Raman spectra obtained from the monometallic Pt thin film between 0.8 and 1.6 V_{RHE} are plotted in Fig. 2b. At 1.0 V_{RHE}, a broad band with a maximum at 558 cm^{-1} is present, while all Raman peaks between 700 and 1000 cm^{-1} disappear. From 1.2 V_{RHE} to higher potentials, a shoulder forms at 725 cm^{-1} and the broad Raman peak at 558 cm^{-1} is retained until 1.3 V_{RHE}. Increasing the potential to 1.4 V_{RHE} results in the formation of a new peak at 675 cm^{-1}, which gradually grows in intensity with higher potential up to 1.6 V_{RHE}.

First, the strong Raman bands between 700 and 1100 cm^{-1} in the potential range of 0.3–1.0 V_{RHE} are associated with surface adsorbed –OH,[50,55] –OOH,[27,49,55] $–HO_2$[50] and $–O_2^-$[27,55] species and the respective peak assignments are summarized in Table S6. The tendency for a potential-induced Raman shift is due to the more amorphous structure and different surface sites present on the rough platinum surface. All of these adsorbed oxygen species are related to ORR intermediates.[56,57] Simultaneously with the formation of adsorbed oxygen species, several bands between 400 and 600 cm^{-1} start to appear from 0.4 V_{RHE} onwards. The observed Raman bands in this region are usually assigned to Pt–O bonds of the Pt oxides.[48] In addition, water adsorbed by the oxygen atom (Pt–OH_2) can also be found at around 500 cm^{-1}.[58]

At 0.8 V_{RHE}, the Raman bands for the adsorbed oxygen species between 700 and 900 cm^{-1} are still more intense compared to those between 400 and 600 cm^{-1} associated with Pt oxide formation (Fig. 2b).[27,48] Thus, a mixture of metallic and oxidized Pt surface is present up to this potential, indicating the formation of some surface oxide species. From 1.0 V_{RHE} to higher potentials, the peaks of the adsorbed oxygen species diminish, while a broad band with a maximum at 558 cm^{-1} appears. As shown by several *in situ* Raman investigations on

Table 2 For the monometallic platinum thin film, Raman peaks and corresponding modes of vibration observed at 1.2 V_{RHE} and 1.6 V_{RHE} in 0.1 M $HClO_4$. Assignments are based on the studies by Huang *et al.*,[27] Zhang *et al.*,[59] and Graham *et al.*[48] and our own DFT calculations

Potential	Raman shift/cm^{-1}	Mode of vibration
1.2 V_{RHE}	558	Amorphous Pt–O; $Pt(OH)_4$ (ref. 27 and 59)
1.6 V_{RHE}	558	Amorphous Pt–O; $Pt(OH)_4$ (ref. 27 and 59)
	600	Pt–O–Pt symmetric stretch
	675	Pt–O–Pt symmetric stretch
	725	Pt_3O_4 (ref. 48)

monometallic platinum, this indicates the formation of amorphous platinum oxide.[27,52,55,59–61] Huang *et al.*[27] and Zhang *et al.*[59] suggested that the OH species are involved in the electrochemical oxide formation on the platinum surface, including those from the surrounding water molecules. Thus, the broad Raman peak at around 550–600 cm^{-1} is assigned to a combination of $Pt(OH)_4$ and amorphous PtO_x, previously reported in both studies.[27,59] Raman peak positions at 1.2 V_{RHE} and 1.6 V_{RHE} with the respective assignments are listed in Table 2.

At 1.3 V_{RHE}, a second peak at 600 cm^{-1} emerges with low intensity that corresponds to the Pt–O–Pt stretch of a hydrated α-PtO_2 type cluster. The peak identification based on our DFT calculations is outlined in the subsequent section. The shoulder at 725 cm^{-1}, which starts to form from 1.2 V_{RHE} and diminishes again at 1.6 V_{RHE}, is ascribed to the Pt_3O_4 oxide containing mixed Pt^{2+} and Pt^{4+} species.[48] This suggests that α-PtO_2 acts as an intermediate for the formation of Pt_3O_4. No further peak shifts and/or other peaks are visible at these anodic potentials. Only from 1.4 V_{RHE} to more positive direction, another Raman band at 675 cm^{-1} appears and is related to the Pt–O–Pt stretch of a hydrated α-PtO_2 type cluster.

To sum up, the Pt thin films show intermediates and precursors of adsorbed (hydr-)oxygen species for the ORR up to 1.0 V_{RHE}. At higher anodic potentials, first amorphous PtO_x forms (broad band at around 558 cm^{-1}), followed by the formation of hydrated α-PtO_2 starting from 1.4 V_{RHE}. At potentials relevant for the OER, a mixture of disordered PtO_x and hydrated α-PtO_2 is detected by the *in situ* Raman data.

3.3.2 *In situ* Raman spectra of the bimetallic PtIr(1 : 1) thin film.

The potential-resolved *in situ* Raman spectra obtained from the bimetallic Pt–Ir thin films were comprehensively investigated during the ORR and OER in 0.1 M $HClO_4$. Similar to the monometallic Ir thin film at low potentials (0.3–0.8 V_{RHE}), the *in situ* Raman spectra for PtIr(1 : 1) are almost identical, showing one sharp Raman band at 568 cm^{-1} (Fig. S13). In contrast to the Pt thin film, no clearly resolved Raman bands between 700 and 1100 cm^{-1} appear in the potential range from 0.3 to 1.0 V_{RHE}. Fig. 3a displays the potential-dependent Raman spectra for the PtIr(1 : 1) thin film between 0.8 and 1.6 V_{RHE}. At

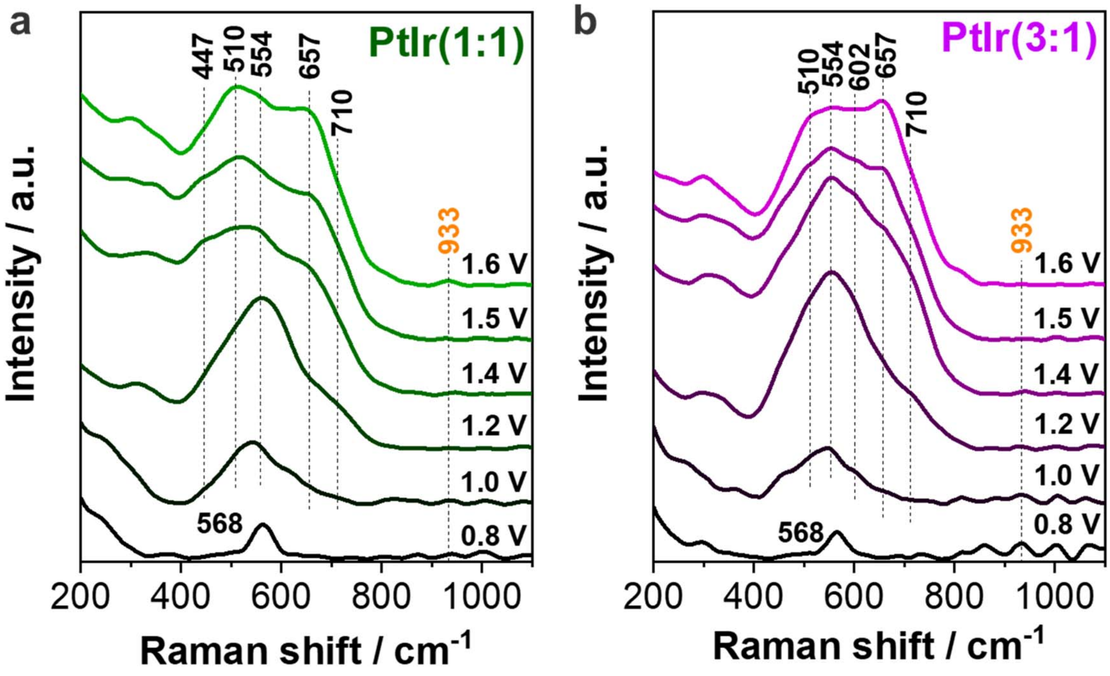

Fig. 3 *In situ* Raman spectra collected from (a) PtIr(1 : 1) and (b) PtIr(3 : 1) thin films in the potential range of 0.8–1.6 V_{RHE} in 0.1 M $HClO_4$. Peak assignments of the respective thin films at 1.2 V_{RHE} and 1.6 V_{RHE} are shown in Tables 3 and 4. The position at 933 cm^{-1} is related to the adsorbed ClO_4^- anion.

1.0 V_{RHE}, the sharp band at 568 cm^{-1} broadens to a more intense peak with a maximum at 554 cm^{-1}, which remains unchanged until 1.2 V_{RHE}. Simultaneously, two smaller bands appear at 301 cm^{-1} and 349 cm^{-1}, indicating an assignment to the same bond. In addition to the bands at 301 cm^{-1}, 349 cm^{-1} and 554 cm^{-1}, only one further shoulder at ~710 cm^{-1} is observed at 1.2 V_{RHE}. The next significant change in the Raman spectrum is observed by applying a potential of 1.4 V_{RHE}. A red-shift of the shoulder into a distinct Raman peak at 657 cm^{-1} and the evolution of two new bands at 447 cm^{-1} and 510 cm^{-1} are clearly visible. Up to 1.6 V_{RHE}, the *in situ* Raman spectra for the PtIr(1 : 1) thin film remain unchanged.

The sharp Raman band observed below 0.8 V_{RHE}, similar to the one obtained for the monometallic Ir thin film, is attributed to Ir^{3+}–OH species.[23,52,53] The absence of bands between 700 and 1100 cm^{-1}, associated with platinum adsorbed –OH,[50,55] –OOH,[27,49,55] $-HO_2$ (ref. 50) and $-O_2^-$,[27,55] indicates the surface enrichment of IrO_x, matching the findings from the *ex situ* XPS data. Since sufficient ORR activity is still present (see Fig. 1d) despite the lack of formation of adsorbed oxygen intermediates, we can conclude that platinum is still in the metallic state. Only from 1.0 V_{RHE} to higher potentials, a broad, more intense Raman peak with a maximum at 554 cm^{-1} appears, which is assigned to the formation of a mixed amorphous Pt–Ir oxide lattice. Note that this bimetallic oxide formation is delayed by 200 mV on the potential scale compared to the monometallic Ir and Pt thin films (Fig. S9). At 1.2 V_{RHE}, an additional shoulder is observed at 710 cm^{-1}, which is attributed to symmetric stretches of the μ-oxo bridging oxygen between Pt and Ir atoms based on our DFT calculations. All Raman band assignments at 1.2 V_{RHE} and 1.6 V_{RHE} are shown in Table 3. Until 1.3 V_{RHE}, these features remain essentially unchanged (Fig. S9c).

From 1.4 V_{RHE} to higher anodic potentials, three new Raman bands at 657 cm^{-1}, 510 cm^{-1} and 447 cm^{-1} appear, indicating changes in the lattice structure as a result of a further electrochemical oxidation of the bimetallic thin film. More precisely, from 1.2 to 1.5 V_{RHE} the band at 710 cm^{-1} shifts to higher energy at 657 cm^{-1}, associated with the Ir–O–Pt stretches of a bimetallic Pt–Ir oxide. This significant red shift indicates the weakening of the Pt–O–Ir bond, accompanying the oxidation of the thin film. The Raman band appearing at 510 cm^{-1} is similar to the Ir–O–Ir stretching vibrations at 498 cm^{-1}, observed for the monometallic Ir thin film. Based on this comparison, we ascribe this peak to the bimetallic Ir–O–Pt stretching frequency that is shifted to lower energy compared to the same frequency of the monometallic Ir thin film. The peak at 447 cm^{-1} corresponds to the respective Ir–O–Pt bending vibration. The peak at 554 cm^{-1} remains constant over this potential range and could originate from an underlying amorphous Pt–Ir oxide phase.

Altogether, the PtIr(1 : 1) thin film shows one broad Raman band with a maximum at 554 cm^{-1} during the ORR (up to 1.2 V_{RHE}), revealing the appearance of an amorphous Pt–Ir oxide. The peaks associated with ORR intermediates, which are observed for the monometallic Pt thin film are completely suppressed due to the surface enrichment of IrO_x. Therefore, the observed high ORR activity is very likely related to the low coverage of the metallic Pt sites with oxygen adsorbates and the surface roughening. In addition, the oxidation of the Ir^{3+}-OH band starts only from 1.0 V_{RHE}, which is significantly delayed on the potential scale by ~200 mV compared to the monometallic Ir thin film. Electrochemical oxidation of the bimetallic film at potentials relevant for the OER results in three main peaks at 510 cm^{-1} (dominant peak), 554 cm^{-1} and 657 cm^{-1}, associated with a bimetallic Pt–O–Ir lattice as well as the underlying amorphous Pt–Ir oxide phase.

3.3.3 Influence of the reduction of Ir content on the ORR and OER intermediates.

To evaluate the effect of a lower Ir content as a costly and very scarce metal on the formation of ORR and OER surface species, potential-resolved *in situ* Raman spectra of the PtIr(3 : 1) thin film were recorded in 0.1 M $HClO_4$ (Fig. 3b). At potentials below 0.8 V_{RHE} (Fig. S14), the same sharp Raman band at 568 cm^{-1} is observed compared to the monometallic Ir and bimetallic PtIr(1 : 1) thin films. Similarly to the PtIr(1 : 1) thin film, no clearly resolved Raman bands between 700 and 1100 cm^{-1} are detected in the potential range from 0.3 to 1.0 V_{RHE}. With increasing the potential to 1.0 V_{RHE}, only a broad Raman peak with a maximum at 554 cm^{-1} appears. This remains unchanged until 1.2 V_{RHE} is applied, where an additional shoulder forms at 710 cm^{-1}. When the potential is further increased to 1.5 V_{RHE}, this Raman frequency is red shifted to 657 cm^{-1}. At 1.5 V_{RHE}, additional peaks (510 cm^{-1} and 602 cm^{-1}) are clearly observed. These peak features are still visible upon applying potentials up to 1.6 V_{RHE}. Obviously, for the PtIr(3 : 1) thin film the most dominant Raman band is observed at 657 cm^{-1} compared to PtIr(1 : 1) at 510 cm^{-1} under similar OER conditions.

We explained the observed Raman bands as a function of the potential as follows. At potentials up to 0.8 V_{RHE}, the sharp Raman band at 568 cm^{-1} is assigned to the presence of Ir^{3+}–OH species, in comparison to the Ir and PtIr(1 : 1) thin films. Similarly, no strong bands for the Pt–O surface species are

Table 3 Potential-dependent Raman peaks and corresponding modes of vibration for the PtIr(1 : 1) thin film at 1.2 V_{RHE} and 1.6 V_{RHE} in 0.1 M $HClO_4$

Potential	Raman shift/cm^{-1}	Mode of vibration
1.2 V_{RHE}	554	Amorphous Pt–Ir oxide
	710	Ir–O–Pt symmetric stretch
1.6 V_{RHE}	447	Ir–O–Pt bend
	510	Ir–O–Pt bend + Ir–O–Pt antisymmetric stretch
	554	Ir–O–Pt bend + Ir–O–Pt antisymmetric stretch
	657	Ir–O–Pt symmetric stretch

Table 4 For the PtIr(3 : 1) thin film, Raman peaks and corresponding modes of vibration at 1.2 V_{RHE} and 1.6 V_{RHE} in 0.1 M $HClO_4$

Potential	Raman shift/cm^{-1}	Mode of vibration
1.2 V_{RHE}	554	Amorphous Pt–Ir oxide
	710	Ir–O–Pt symmetric stretch + Pt–O–Pt symmetric stretch
1.6 V_{RHE}	510	Ir–O–Pt bend + Ir–O–Pt antisymmetric stretch
	550	Ir–O–Pt bend + Ir–O–Pt antisymmetric stretch
	602	Ir–O–Pt symmetric stretch + Pt–O–Pt symmetric stretch
	657	Ir–O–Pt symmetric stretch + Pt–O–Pt symmetric stretch

detected between 700 and 1100 cm^{-1}. This is very surprising, because of the high platinum content (75 at%) in the PtIr(3 : 1) thin film. However, the strong oxophilicity of surface-enriched IrO_x suppresses the adsorption of oxygen-based species on platinum. With increasing the potential to 1.0 V_{RHE}, a broad Raman peak with a maximum at 554 cm^{-1} appears, which is associated with the formation of an amorphous Pt–Ir oxide. At 1.2 V_{RHE}, a weak shoulder develops at around 710 cm^{-1} (Table 4) and corresponds to bridging Ir–O–Pt stretches of a bimetallic Pt–Ir oxide.

In general, the Raman band structure after additional electrochemical oxidation from 1.4 V_{RHE} to higher potentials is different from that of PtIr(1 : 1), except for the Raman band at 657 cm^{-1}, which is observed for both thin films. In contrast to PtIr(1 : 1), this distinct peak becomes the most intense band at 1.6 V_{RHE} (OER) in the Raman spectrum for the PtIr(3 : 1) thin film and corresponds to Ir–O–Pt stretches. A further peak, which has not been observed for PtIr(1 : 1), appears at 602 cm^{-1} upon applying a potential equal to or higher than 1.4 V_{RHE}. Based on the results from the monometallic Pt thin film, we assigned this peak to the Pt–O stretching frequency of the monometallic hydrated α-PtO_2. The tendency for platinum oxide formation is more pronounced for PtIr(3 : 1) due to the higher Pt surface concentration (see *ex situ* XPS, Fig. 1c). Furthermore, the band at 510 cm^{-1} only becomes observable with a low intensity at potentials above 1.5 V_{RHE}, indicating some structural differences between the Pt–Ir oxide species formed with different atomic Pt : Ir ratios.

Altogether, during the ORR the *in situ* Raman spectrum of the PtIr(3 : 1) thin film shows mainly one broad peak at 554 cm^{-1} that corresponds to an amorphous Pt–Ir oxide. Similar to the PtIr(1 : 1) thin film, the absence of adsorbed ORR intermediates on the Pt sites is observed due to the increased presence of the IrO_x surface. At 1.6 V_{RHE} (OER), several Raman peaks at 510, 554, 602 and 657 cm^{-1} are detected, related to the formation of bimetallic Pt–Ir oxide species. The band at 657 cm^{-1} associated with the Ir–O–Pt stretching frequency of a bimetallic Pt–Ir oxide is the most dominant in the Raman spectrum, while the band at 602 cm^{-1} is associated with monometallic hydrated α-PtO_2.

3.4. DFT calculations of Ir, Pt and Pt–Ir model clusters

Density functional theory (DFT) calculations were conducted to obtain a better understanding of the catalytically active Pt–Ir sites for the ORR and OER. Calculations of the model structures and predicted Raman spectra are based on the μ-oxo bridge-connected IrO_6 octahedra as a simple model proposed by Pavlovic *et al.*,[22] which yields a good agreement with experimental data in their study. The model follows a cluster modelling approach, which can be understood as a cutout of the periodic rutile-IrO_2 structure. Since this methodology creates unsaturated dangling oxygen bonds, hydrogen atoms are used to fully coordinate them and balance charges. In this way, either OH or H_2O groups are formed to coordinate them around the metal centers. The terminating hydroxy groups were attached to the bottom side of the metal centers as well as the axial dangling bonds to simulate a polymeric oxide structure. On the other hand, the top side was saturated with water to mimic the surface. Four different cluster systems were theoretically modeled, which are rutile-IrO_2, α-PtO_2 and two bimetallic Pt–Ir oxides with a rutile structure of Pt : Ir ratios of 1 : 1 and 3 : 1. In order to optimize the computational efforts, the smallest cluster sizes were defined as tetramers, to model the system with sufficient accuracy. To ensure the validity of this approach, we modelled a larger IrO_2 cluster model, a 2D octamer with 67 atoms (Fig. S15) and calculated the Raman spectrum. In Fig. S16, all the main features of the Raman spectrum remain when the model size is increased. A shift of the main vibrational Ir–O–Ir stretching bands can be observed, bringing them closer together. Since the same behavior can be expected for all cluster models, the relative difference between the two main vibration bands remains unchanged. Due to the minor changes in Raman band positions and adequate computational effort per cluster size, we concluded that tetramers are still sufficient and meaningful for predicting the Raman spectra. In agreement with the work by Pavlovic *et al.*,[22] when using dimers as model structures, the intensities could be very low, making the comparison very difficult. In their study, trimers were employed to model the IrO_x system and were found to successfully replicate important features of the experimental Raman spectra.

First, geometry optimizations were performed on the four tetramer models such as Ir–Ir–Ir–Ir, Pt–Pt–Pt–Pt, Ir–Pt–Ir–Pt and Pt–Pt–Ir–Pt. Thereby, the hydrogen atoms were optimized, while all other atoms were constrained. The –OH groups at the bottom of the cluster were then fixed to simulate the bulk phase and the upper layer was completely relaxed. The final and stable geometries of all oxo-hydroxo tetramer models are illustrated in Fig. 4.

The average Ir–O bond distance in the monometallic iridium tetramer system is 1.85–2.06 Å, while the distance of Ir–H_2O is between 2.23 and 2.28 Å. For α-PtO_2, these values are 1.95–2.00 Å and 2.18–2.20 Å, respectively. In general, the Pt–O bond

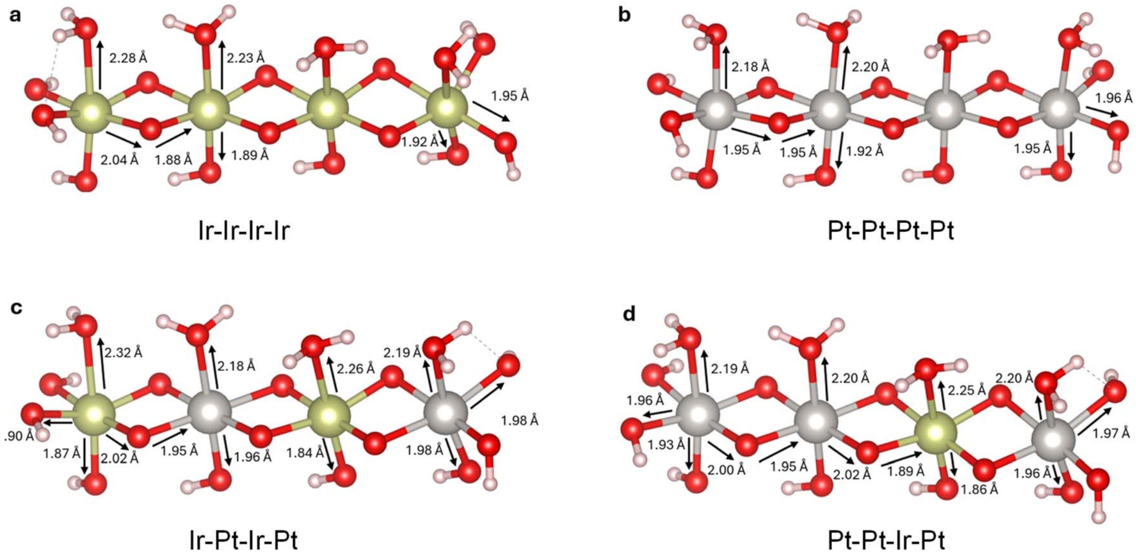

Fig. 4 Optimized tetramer geometries of the (a) iridium oxo-hydroxo complex, (b) platinum oxo-hydroxo complex and (c and d) bimetallic platinum–iridium oxo-hydroxo complexes with (c) 1 : 1 and (d) 3 : 1 Pt : Ir ratios employed for the calculations of the predicted Raman spectra. Iridium, platinum, oxygen and hydrogen are denoted with gold, silver, red and white spheres, respectively. For each cluster, the most important calculated bond lengths are shown. For geometry optimization, the bottom –OH groups were fixed, allowing only the μ-oxo bridges and top-side H_2O molecules to freely move.

distances are shorter, indicating stronger bonding to oxygen. The Ir–O–Pt bonds in the mixed clusters show bond lengths from 1.84–2.06 Å. Obviously, there is no clear tendency for either Ir–O or Pt–O bonds to be longer or shorter in the mixed cluster. On the other hand, the water ligands show a clear difference in average bond lengths of 2.28 Å and 2.18 Å for the monometallic iridium and platinum centers, respectively.

Raman spectra were calculated for all optimized oxo-hydroxo tetramer clusters, while the bottom –OH groups were fixed, allowing only the μ-oxo bridges and top-side H_2O molecules to freely move. The predicted spectra of these four tetramer clusters are displayed in Fig. 5. A list of the most prominent peaks of the calculated Raman frequencies and corresponding vibrations is given in Tables S7 to S10. It is noted that for all complexes, the strong vibrations of the bridging μ-oxo bonds show the most prominent peaks in the DFT-predicted Raman spectra (Fig. S17–S20).

In Fig. 5a, the Raman spectrum of the iridium oxo-hydroxo complex is displayed. The monometallic iridium oxide model is dominated by two distinct peaks at 525 cm^{-1} and 725 cm^{-1}, which can be attributed to antisymmetric and symmetric Ir–O–Ir stretching vibrations (Fig. S17), respectively. Compared to the iridium oxide model, the platinum oxo-hydroxo complex based on the α-PtO_2 structure has far less pronounced peaks, as shown in Fig. 5b. The four distinct high intensity vibrations appear as an integration of broad peaks between 500 and 650 cm^{-1}. The vibrations are on average at a lower wavelength compared to those of the monometallic iridium oxide cluster. In all high intensity vibrational modes (505, 572, 606 and 645 cm^{-1}), the Pt–O–Pt bending motions are observed to some degree, while the dominant contribution originates from the symmetric stretching vibrations (Fig. S18).

In Fig. 5c, the calculated Raman spectrum of the mixed platinum–iridium oxo-hydroxo complex with a Pt : Ir ratio of 1 : 1 shows a large variety of high intensity peaks with Ir–O–Pt bending vibrations (Fig. S19). More precisely, the most dominant peak appears at approximately 600 cm^{-1}, while weaker bending vibrations are found between 400 and 500 cm^{-1}. Some antisymmetric stretching is observed at approximately 550 cm^{-1}. Of special interest is the range between 600 and 700 cm^{-1}, which is composed of three different intense vibrations. It is noted that these individual vibrations are indistinguishable in the Raman spectrum due to the peak integration. All these vibrations have major contributions from the symmetric Ir–O–Pt stretching motions. Peaks in this range of wavelengths are either absent or only partly covered in the calculated monometallic platinum and iridium oxo-hydroxo complexes, leading to new Raman band structures not observed for the monometallic platinum and iridium oxo-hydroxo complexes.

For the mixed platinum–iridium oxo-hydroxo complex with the central atom structure of Pt–Pt–Ir–Pt, the predicted Raman spectrum shows multiple peaks similar to those of the 1 : 1 Pt : Ir cluster model, as shown in Fig. 5d. Due to additional Pt–O–Pt interactions, some new frequencies emerge, for example, at 507 cm^{-1}. In addition to the Pt–O–Ir stretching and bending vibrations, major contributions of μ-oxo bridged Pt–O–Pt stretching and bending motions are clearly seen between 600 and 700 cm^{-1} (Fig. S20). Furthermore, a shift in intensities is highlighted by comparing platinum–iridium oxo-hydroxo clusters of 1 : 1 and 3 : 1 ratios. More precisely, the most intense peak for the Ir–Pt–Ir–Pt oxo-hydroxo cluster appears at around 600 cm^{-1}. In contrast, the Pt–Pt–Ir–Pt oxo-hydroxo cluster shows the highest intensity at 515 cm^{-1}, which is likely caused

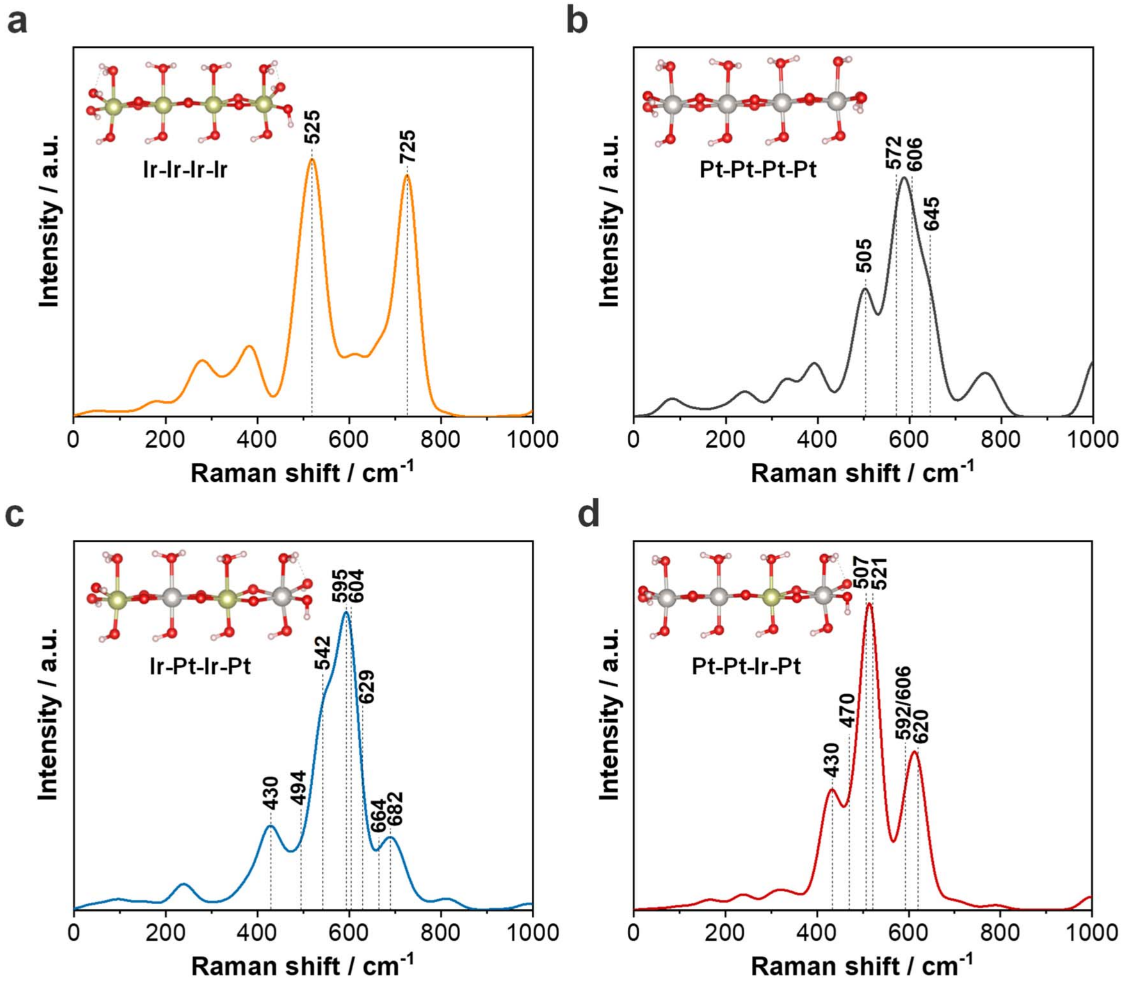

Fig. 5 DFT-based calculated Raman spectra of the tetramer complexes of (a) iridium oxo-hydroxo, (b) platinum oxo-hydroxo and (c and d) bimetallic platinum–iridium oxo-hydroxo with Pt : Ir ratios of (c) 1 : 1 and (d) 3 : 1. Assignments of the Raman frequencies to the respective motions are displayed in Tables S7–S10. Note that individual vibrations become noticeable as an integration in a broad Raman band.

by the larger proportion of lower energy of the Pt–O–Pt vibrations.

To summarize, we constructed tetrameric iridium, platinum and two bimetallic platinum–iridium oxo-hydroxo model clusters based on DFT calculations. The metal centers are connected by μ-oxo bridge linkages. The calculated Raman spectra of the monometallic clusters are significantly different from the bimetallic ones, due to the variations of the bending and stretching frequencies of the strong μ-oxo bridge vibrations. For the bimetallic cluster with a 3 : 1 Pt : Ir ratio, additional monometallic Pt–O–Pt bending and stretching motions contribute to the Raman spectrum.

4. Discussion

In this work, the potential-dependent formation of the catalytically active sites of bimetallic Pt–Ir thin films and their electronic structure were comprehensively evaluated for the ORR and OER using *in situ* Raman spectroscopy and DFT. In general, *in situ* Raman spectroscopy is a powerful technique to uncover the differences in ORR and OER activities between the bimetallic and monometallic surfaces based on the nature of vibrations, bond strengths and oxygen coverage.

First, our results demonstrate that the Pt–Ir, Pt and Ir thin films exhibit rough and significantly oxidized surfaces. For both PtIr(1 : 1) and PtIr(3 : 1), *ex situ* XPS analysis reveals a surface enrichment of iridium compared to the bulk. The electrochemical activity data pointed out a superior activity towards the ORR for the Pt–Ir thin films, while their OER activity is still sufficient, confirming the bifunctionality to accelerate both reactions. In other words, the OER activity strongly reduces with a decreasing amount of iridium and the observed ORR activity is the highest for the bimetallic PtIr(3 : 1) thin film. *Ex situ* Raman spectra of the thin films show the presence of mostly disordered amorphous Pt and Ir oxides, while all iridium containing films also have two distinct bands for the rutile IrO_2 structure (E_g and B_{2g}). These findings indicate the existence of two separate Pt oxide and Ir oxide phases at the surface of the bimetallic PtIr(1 : 1) and PtIr(3 : 1) thin films under ambient conditions. The formation of these separate phases is most likely related to the alternating sputter process of Ir and Pt without heating.

4.1. *In situ* Raman spectroscopy data before and during the ORR (0.3 to 1.2 V_{RHE})

Between 0.3 and 0.8 V_{RHE}, the bimetallic PtIr(1 : 1) and PtIr(3 : 1) thin films exhibit a similar behavior to that of monometallic Ir. All of them show a sharp band, associated with highly stabilized Ir^{3+}–OH species at 564 cm^{-1} and 568 cm^{-1}, respectively. The Raman spectrum of the Ir film at 0.8 V_{RHE} shows significant broadening around the sharp band at 564 cm^{-1}, together with the evolution of a new band at 498 cm^{-1}. These are associated with the μ-oxo bond of Ir^{4+} centers.[22] In contrast, the bimetallic thin films do not show the formation of a broad peak until 1.0 V_{RHE}, indicating a higher activation barrier for the electrochemical oxidation of Ir^{3+} to Ir^{4+} in these atomic arrangements.

Due to the absence of further peaks in the Raman spectrum of the bimetallic films between 0.3 and 0.8 V_{RHE}, we conclude that platinum is fully reduced to the metallic state. Based on our recent DFT calculations, the adsorption of oxygen preferentially occurs on the Ir-rich FCC sites of bimetallic PtIr(111) and $Pt_3Ir(111)$ surfaces.[21] Furthermore, the presence of Ir^{3+}-OH surface species for bimetallic thin films suppresses the adsorption of observable ORR intermediates like –OOH, –OH, –O_2^- and –HO_2 species on the active Pt sites.[27,49,50,55] The monometallic Pt film already shows ORR intermediates between 700 and 1100 cm^{-1}, when a potential is applied from 0.3 to 0.8 V_{RHE}. Interestingly, the low coverage of oxygen-containing adsorbates on the active Pt sites and high surface roughness might be the cause of the superior ORR activity for PtIr(3 : 1) compared to monometallic Pt and PtIr(1 : 1).

Very interestingly, at 1.0 V_{RHE} an amorphous Pt–Ir oxide is formed on the surface of the PtIr(1 : 1) and PtIr(3 : 1) thin films, as evidenced by the broad Raman band with a maximum at 554 cm^{-1}. This broad band closely resembles that observed for the monometallic Pt film (at around 558 cm^{-1}), but is slightly blue shifted to a lower frequency. Up to 1.3 V_{RHE}, the Raman spectra of the Pt and Pt–Ir thin films remain essentially unchanged. In contrast, the Raman peaks for the monometallic Ir film appear in a much broader frequency range and tend to shift with the applied potential between 0.8 and 1.2 V_{RHE}, indicating the formation of more flexibly bound oxygen species within IrO_x compared to a rigid crystalline IrO_2 lattice.[22,54]

Altogether, at potentials below 0.8 V_{RHE} mixed Ir^{3+}-OH and metallic Pt are observed at the surface of the bimetallic thin films. These neighboring Ir^{3+}-OH species reduce the coverage of ORR intermediate species on the low-coordinated active Pt sites, resulting in enhanced ORR kinetics.

4.2. *In situ* Raman spectroscopy data before and during the OER (1.3 to 1.6 V_{RHE})

In general, thermodynamically stable crystalline rutile IrO_2 forms under OER conditions.[21,28] The Raman bands are located at 561, 728 and 752 cm^{-1}, corresponding to E_g, B_{2g} and A_{1g}, respectively.[46,47] On the other hand, PtO_2 exists in two structures, namely α-PtO_2 and β-PtO_2. The two strong Raman peaks observed at 511 cm^{-1} (A_{1g}) and 550 cm^{-1} (E_g) are ascribed to the formation of the thermodynamically stable α-PtO_2 under OER conditions.[21,27,28,48]

Before the OER sets in, the second oxidation wave commences at 1.4 V_{RHE} and is anodically shifted by 100 mV for the bimetallic PtIr(1 : 1) thin film compared to monometallic Ir (1.3 V_{RHE}). Mainly, three new Raman bands at ∼510 cm^{-1}, ∼550 cm^{-1} and 657 cm^{-1} appear, which do not change up to 1.6 V_{RHE} and are different from those observed for both monometallic Pt and Ir. Very importantly, our experimental data and DFT calculations point out that the potential-induced formation of bimetallic Pt–O–Ir phases occurs, where the predicted Pt–O–Ir stretching and bending vibrations are estimated to be at three distinct peaks at 542 cm^{-1}, ∼600 cm^{-1} and ∼682 cm^{-1}. This observation is clearly different from the appearance of monometallic Ir or Pt oxides during the OER. Therefore, we can conclude that the OER kinetics are governed by the platinum–iridium oxo-hydroxo structure as the catalytically active site for the PtIr(1 : 1) thin film.

From 1.5 V_{RHE} to higher potentials, an increase in platinum concentration for the PtIr(3 : 1) thin film results in distinct Raman peaks at ∼510 cm^{-1}, ∼550 cm^{-1}, ∼602 cm^{-1} and 657 cm^{-1}, indicating structural differences in the surface oxide compared to both monometallic and PtIr(1 : 1) films. However, the peak at 510 cm^{-1} is much less pronounced compared to the other bands. To get an understanding of the observed Raman bands, we calculated a cluster with three Pt centers and one Ir center (Pt–Pt–Ir–Pt). As a result, the contributions of Pt–O–Pt stretching and bending frequencies combined with Pt–O–Ir stretching frequencies lead to a slight red shift of the Raman bands compared to the Ir–Pt–Ir–Pt cluster, indicating the weakening of Pt–O compared to the Ir–O bond. Similar to monometallic Pt, stronger contributions of the Pt–O–Pt bending frequencies to the calculated Raman bands are observed. Based on these findings, we were able to clearly assign the additional experimental Raman band at 602 cm^{-1} to the Pt–O–Pt stretching frequency. Therefore, the PtIr(3 : 1) thin film shows the potential-induced formation of Pt–O–Pt and Pt–O–Ir surface species from 1.3 to 1.6 V_{RHE}.

4.3. Comparison between experiments and DFT calculations during the OER

In principle, both bimetallic Pt–Ir thin films show very similar Raman bands at ∼510 cm^{-1}, 554 cm^{-1} and 657 cm^{-1} (Fig. 6a) during the OER (1.6 V_{RHE}). A detailed comparison between the experimental and theoretical data is listed in Table S11. The two bands at around 510 cm^{-1} and 554 cm^{-1} are assigned to Pt–O–Ir μ-oxo stretching motions of a bimetallic Pt–Ir oxide surface. The plateau between 600 and 650 cm^{-1} comprises several Raman bands and indicates the presence of a monometallic hydrated α-PtO_2 phase, as shown by a comparison of the Raman spectra of the PtIr(3 : 1) and monometallic Pt films. The most pronounced Raman band is still observed at 657 cm^{-1} for both PtIr(1 : 1) and PtIr(3 : 1). Very remarkably, this peak is red shifted to lower energy by 38 cm^{-1} (≈0.48 kJ mol^{-1}) compared to the same Ir–O–Ir band at 695 cm^{-1}, highlighting a change in the metal–oxygen bond strength between monometallic Ir and Pt–O–Ir bond. In the DFT-predicted Raman spectra (Fig. 6b), the Ir–O–Ir stretching frequency is found at 725 cm^{-1}, while this band is

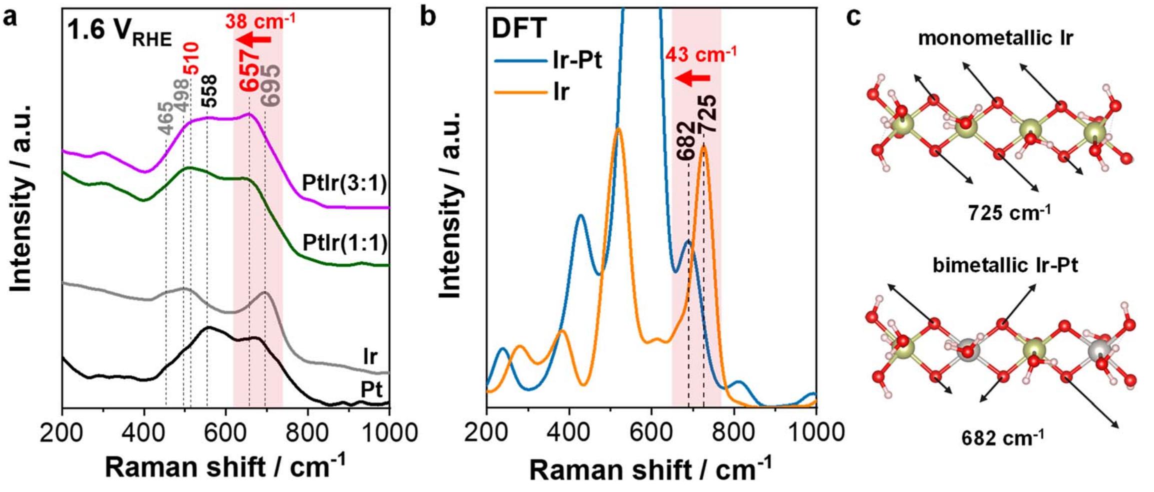

Fig. 6 Comparison between experiments and theoretical DFT calculations. (a) *In situ* Raman spectra of all bimetallic Pt–Ir as well as monometallic Pt and Ir thin films recorded at 1.6 V_{RHE} in 0.1 M $HClO_4$. (b) Computed Raman spectra of the monometallic iridium oxo-hydroxo complex (orange) and bimetallic platinum–iridium oxo-hydroxo complex (blue). (c) Vibrations of the strong movement of the μ-oxo bonds corresponding to the Raman frequencies at 725 cm^{-1} (monometallic Ir complex) and 682 cm^{-1} (bimetallic Ir–Pt complex). The arrows show the direction and magnitude of the atomic movement.

red shifted by 43 cm^{-1} to 682 cm^{-1} for the bimetallic cluster. The main vibrations contributing to these two frequencies are shown in Fig. 6c and arise from the strong μ-oxo bond stretching motions of the respective complexes.

Based on this significant red shift, we can highlight that the relative reduction in the bond strength is around ∼13% and most likely caused by the weakening and lengthening of the Ir–O–Pt bond compared to the Ir–O–Ir bond. This weaker and longer metal–oxygen bond by around 0.48 kJ mol^{-1} in the bimetallic thin films results in the observed decrease in OER activity. According to the Sabatier principle,[62] the Ir–O–Pt bond seems to be too weak compared to the Ir–O–Ir bond, highlighting the need for an optimum binding strength to accelerate the OER kinetics and resulting in a so-called volcano plot. For instance, rutile-IrO_2 has a much stronger –O* binding compared to α-PtO_2, which is beneficial for improving the OER kinetics.[63,64] In addition, a shortening of the Ir–O bond length results in an activity enhancement.[53,54,65–68] To sum up, the Pt–O–Ir bond strength is reduced by about 13% compared to Ir–O–Ir. The weakening of the μ-oxo bond correlates with changes in the OER activity. In other words, Pt–Ir is not as active as IrO_x, but it is much more active than Pt.

Overall, the *in situ* Raman and DFT investigations provide new structural insights into the potential-resolved formation of catalytically active sites for bimetallic Pt–Ir surfaces for both the ORR and OER. Independent of the Pt : Ir ratio, the presence of Ir^{3+}–OH reduces the coverage of adsorbed oxygen intermediates on the Pt sites, resulting in an enhancement of ORR activity. At potentials higher than 1.0 V_{RHE}, amorphous Pt–Ir oxides appear for the first time. A further increase in the potential induces the formation of platinum–iridium oxo-hydroxo type structures instead of separate monometallic Ir and Pt oxide phases. Very remarkably, the unique combination of surface-sensitive *in situ* Raman spectroscopy and DFT calculations reveals the lower OER kinetics of the bimetallic surface by weakening of the Ir–O–Pt bond compared to monometallic IrO_x.

5. Conclusion

In this work, we investigated the potential-dependent oxidation of sputtered bifunctional Pt–Ir thin films as a model catalyst system for the ORR and OER using *in situ* Raman spectroscopy and DFT. The evaluation of the electrochemical activity data highlights the ORR/OER bifunctionality of these bimetallic Pt–Ir thin films.

In situ Raman spectroscopy is a powerful technique to identify the reaction intermediates on metal-based surfaces. At potentials below 0.8 V_{RHE}, the surface of the bimetallic Pt–Ir thin films contains highly stable Ir^{3+}-OH, which prevents the adsorption of oxygen-containing species onto the active Pt sites. At 1.0 V_{RHE}, the first oxidation wave commences with the formation of an amorphous Pt–Ir oxide, which is evident by a broad Raman band at ∼554 cm^{-1}. This is shifted by 200 mV compared to that of the monometallic Ir film, where peak broadening occurred already at 0.8 V_{RHE}, indicating electronic interactions between platinum and iridium to improve the ORR kinetics. For the PtIr(1 : 1) thin film, the second oxidation wave commences from 1.4 V_{RHE} to higher potentials relevant for the OER, showing strong changes in the bimetallic oxide structure compared to monometallic Pt and Ir. DFT was used to calculate the Raman spectra for two hydrated platinum–iridium oxo-hydroxo tetramer complexes, where the Pt and Ir atoms are connected to each other by μ-oxo type linkage. Based on the predicted Raman spectra, we could show that the experimental peaks observed correspond to Pt–O–Ir stretching and bending vibrations. One of these stretching frequencies is observed at 657 cm^{-1}, which is red shifted by ∼38 cm^{-1} from the same vibration for monometallic Ir–O–Ir. This shift in the Raman frequency is most likely based on a weakening of the Ir–O–Pt bond by 13% compared to that of the monometallic Ir–O–Ir bond, resulting in a lower OER activity of the bimetallic Pt–Ir thin films. Therefore, a critical tuning of μ-oxo bond linkages of the metal centers is the key to accelerating the OER.

The unique combination of *in situ* Raman and DFT allows uncovering a new mechanistic understanding of the potential-resolved formation of catalytically active sites of bimetallic Pt–Ir materials for the ORR and OER. This knowledge will help boost the performance of unitized regenerative fuel cells in the near future.

Conflicts of interest

There are no conflicts to declare.

Data availability

The data supporting this article have been included as part of the supplementary information (SI). Supplementary information: additional experimental and calculated Raman spectra, schematic illustrations of vibrational modes, electrochemical data such as cyclic voltammograms, as well as SEM, XRD, and XPS data. See DOI: https://doi.org/10.1039/d6ta01745b.

Acknowledgements

The authors would like to acknowledge the Federal Ministry of Research, Technology and Space (BMFTR) for funding the project EcatPEMFCplus (03SF0617A) and EcatPEMFCmaritim (03SF0645), as well as the German Research Foundation (DFG) for funding the WITec alpha300 RSA confocal microscope (INST 188/517-1 FUGG) and XPS instrument (INST 184/144-1 FUGG). Part of the simulations were performed at the HPC Cluster ROSA, located at the University of Oldenburg (Germany) and funded by the DFG through its Major Research Instrumentation Program (INST 184/225-1 FUGG) and the Ministry of Science and Culture (MWK) of the Lower Saxony State. In addition, we thank Tammo Stein for the support with the design of the electrochemical Raman cell.

References

1 J. Du, J. Quinson, D. Zhang, F. Bizzotto, A. Zana and M. Arenz, Bifunctional Pt-IrO$_2$ Catalysts for the Oxygen Evolution and Oxygen Reduction Reactions: Alloy Nanoparticles versus Nanocomposite Catalysts, *ACS Catal.*, 2021, **11**(2), 820–828, DOI: 10.1021/acscatal.0c03867.

2 S.-Y. Huang, P. Ganesan, H.-Y. Jung and B. N. Popov, Development of supported bifunctional oxygen electrocatalysts and corrosion-resistant gas diffusion layer for unitized regenerative fuel cell applications, *J. Power Sources*, 2012, **198**, 23–29, DOI: 10.1016/j.jpowsour.2011.09.071.

3 J.-H. Kim, S.-W. Yun, K. Shim, S.-H. You, S.-M. Jung, H. Kweon, S. H. Joo, Y. H. Moon and Y.-T. Kim, Enhanced Activity and Stability of Nanoporous PtIr Electrocatalysts for Unitized Regenerative Fuel Cell, *ACS Appl. Energy Mater.*, 2020, **3**(2), 1423–1428, DOI: 10.1021/acsaem.9b01874.

4 S. Morales, Y. Gochi-Ponce, A. Altamirano-Gutiérrez and A. M. Fernández, Influence of the Pt$_x$RuIr$_y$ electrocatalysts composition toward oxygen evolution and reduction reactions for unitized regenerative fuel cell, *Int. J. Hydrogen Energy*, 2021, **46**(51), 26019–26026, DOI: 10.1016/j.ijhydene.2021.03.197.

5 S. Wang, A. Z. Weber and X. Peng, Advances and prospects to achieve high-performing and durable proton-exchange-membrane unitized regenerative fuel cells, *Curr. Opin. Electrochem.*, 2023, **40**, 101340, DOI: 10.1016/j.coelec.2023.101340.

6 F. Mitlitsky, B. Myers and A. H. Weisberg, Regenerative Fuel Cell Systems, *Energy Fuels*, 1998, **12**, 56–71.

7 Y. N. Regmi, X. Peng, J. C. Fornaciari, M. Wei, D. J. Myers, A. Z. Weber and N. Danilovic, A low temperature unitized regenerative fuel cell realizing 60% round trip efficiency and 10 000 cycles of durability for energy storage applications, *Energy Environ. Sci.*, 2020, **13**(7), 2096–2105, DOI: 10.1039/C9EE03626A.

8 X. Peng, Z. Taie, J. Liu, Y. Zhang, X. Peng, Y. N. Regmi, J. C. Fornaciari, C. Capuano, D. Binny, N. N. Kariuki, D. J. Myers, M. C. Scott, A. Z. Weber and N. Danilovic, Hierarchical electrode design of highly efficient and stable unitized regenerative fuel cells (URFCs) for long-term energy storage, *Energy Environ. Sci.*, 2020, **13**(12), 4872–4881, DOI: 10.1039/D0EE03244A.

9 T. Sadhasivam, K. Dhanabalan, S.-H. Roh, T.-H. Kim, K.-W. Park, S. Jung, M. D. Kurkuri and H.-Y. Jung, A comprehensive review on unitized regenerative fuel cells: Crucial challenges and developments, *Int. J. Hydrogen Energy*, 2017, **42**(7), 4415–4433, DOI: 10.1016/j.ijhydene.2016.10.140.

10 T. C. Crowtz and J. R. Dahn, Screening Bifunctional Pt Based NSTF Catalysts for Durability with the Rotating Disk Electrode: The Effect of Ir and Ru, *J. Electrochem. Soc.*, 2018, **165**(10), F854–F862, DOI: 10.1149/2.0891810jes.

11 H.-Y. Jung, S. Park and B. N. Popov, Electrochemical studies of an unsupported PtIr electrocatalyst as a bifunctional oxygen electrode in a unitized regenerative fuel cell, *J. Power Sources*, 2009, **191**(2), 357–361, DOI: 10.1016/j.jpowsour.2009.02.060.

12 T. Ioroi and K. Yasuda, Platinum-Iridium Alloys as Oxygen Reduction Electrocatalysts for Polymer Electrolyte Fuel Cells, *J. Electrochem. Soc.*, 2005, **152**(10), A1917, DOI: 10.1149/1.2006547.

13 L. Blanco-Redondo, Y. Lobko, K. Veltruská, J. Nováková, M. Mazur, A. M. Darabut, T. Hrbek, M. Dopita, J. Hraníček, Y. Yakovlev, I. Matolínová and V. Matolín, Bifunctional Pt–Ir nanoparticle catalysts for oxygen reduction and evolution reactions: investigating the influence of surface composition on the catalytic properties, *Sustainable Energy Fuels*, 2024, **8**(4), 797–810, DOI: 10.1039/D3SE01238G.

14 M. Wesselmark, B. Wickman, C. Lagergren and G. Lindbergh, The impact of iridium on the stability of

platinum on carbon thin-film model electrodes, *Electrochim. Acta*, 2013, **111**, 152–159, DOI: 10.1016/j.electacta.2013.07.108.

15 G. C. Da Silva, K. J. J. Mayrhofer, E. A. Ticianelli and S. Cherevko, Dissolution Stability: The Major Challenge in the Regenerative Fuel Cells Bifunctional Catalysis, *J. Electrochem. Soc.*, 2018, **165**(16), F1376–F1384, DOI: 10.1149/2.1201816jes.

16 T. Zhang, S.-C. Li, W. Zhu, Z.-P. Zhang, J. Gu and Y.-W. Zhang, Shape-tunable Pt-Ir alloy nanocatalysts with high performance in oxygen electrode reactions, *Nanoscale*, 2017, **9**(3), 1154–1165, DOI: 10.1039/C6NR08359E.

17 M. Scohy, S. Abbou, V. Martin, B. Gilles, E. Sibert, L. Dubau and F. Maillard, Probing Surface Oxide Formation and Dissolution on/of Ir Single Crystals via X-ray Photoelectron Spectroscopy and Inductively Coupled Plasma Mass Spectrometry, *ACS Catal.*, 2019, **9**(11), 9859–9869, DOI: 10.1021/acscatal.9b02988.

18 M. Wakisaka, H. Suzuki, S. Mitsui, H. Uchida and M. Watanabe, Identification and quantification of oxygen species adsorbed on Pt(111) single-crystal and polycrystalline Pt electrodes by photoelectron spectroscopy, *Langmuir*, 2009, **25**(4), 1897–1900, DOI: 10.1021/la803050r.

19 R. Mom, L. Frevel, J.-J. Velasco-Vélez, M. Plodinec, A. Knop-Gericke and R. Schlögl, The Oxidation of Platinum under Wet Conditions Observed by Electrochemical X-ray Photoelectron Spectroscopy, *J. Am. Chem. Soc.*, 2019, **141**(16), 6537–6544, DOI: 10.1021/jacs.8b12284.

20 Y. B. He, A. Stierle, W. X. Li, A. Farkas, N. Kasper and H. Over, Oxidation of Ir(111): From O-Ir-O Trilayer to Bulk Oxide Formation, *J. Phys. Chem. C*, 2008, **112**, 11946–11953, DOI: 10.1021/jp803607y.

21 T. Wittemann, H. İ. Sözen, M. Oezaslan and T. Klüner, Ab initio calculations of the chemisorption of atomic H and O on Pt and Ir metal and on bimetallic Pt_xIr_y surfaces, *Z. Naturforsch. B*, 2024, **79**(4), 177–190, DOI: 10.1515/znb-2023-0087.

22 Z. Pavlovic, C. Ranjan, Q. Gao, M. van Gastel and R. Schlögl, Probing the Structure of a Water-Oxidizing Anodic Iridium Oxide Catalyst using Raman Spectroscopy, *ACS Catal.*, 2016, **6**(12), 8098–8105, DOI: 10.1021/acscatal.6b02343.

23 Z. Pavlovic, C. Ranjan, M. van Gastel and R. Schlögl, The active site for the water oxidising anodic iridium oxide probed through in situ Raman spectroscopy, *Chem. Commun.*, 2017, **53**(92), 12414–12417, DOI: 10.1039/C7CC05669A.

24 F. Zhao, B. Wen, W. Niu, Z. Chen, C. Yan, A. Selloni, C. G. Tully, X. Yang and B. E. Koel, Increasing Iridium Oxide Activity for the Oxygen Evolution Reaction with Hafnium Modification, *J. Am. Chem. Soc.*, 2021, **143**(38), 15616–15623, DOI: 10.1021/jacs.1c03473.

25 S. P. Devarajan, J. A. Hinojosa and J. F. Weaver, STM study of high-coverage structures of atomic oxygen on Pt(111): p(2×1) and Pt oxide chain structures, *Surf. Sci.*, 2008, **602**(19), 3116–3124, DOI: 10.1016/j.susc.2008.08.008.

26 J. M. Hawkins, J. F. Weaver and A. Asthagiri, Density functional theory study of the initial oxidation of the Pt(111) surface, *Phys. Rev. B*, 2009, **79**, 125434, DOI: 10.1103/PhysRevB.79.125434.

27 Y.-F. Huang, P. J. Kooyman and M. T. M. Koper, Intermediate stages of electrochemical oxidation of single-crystalline platinum revealed by in situ Raman spectroscopy, *Nat. Commun.*, 2016, **7**(1), 12440, DOI: 10.1038/ncomms12440.

28 A. Kafka and F. Hess, Why alloying with noble metals does not decrease the oxidation of platinum: a DFT-based ab initio thermo-dynamics study, *Phys. Chem. Chem. Phys.*, 2024, **26**(37), 24631–24648, DOI: 10.1039/D4CP01807A.

29 G. W. Sievers, A. W. Jensen, J. Quinson, A. Zana, F. Bizzotto, M. Oezaslan, A. Dworzak, J. J. K. Kirkensgaard, T. E. L. Smitshuysen, S. Kadkhodazadeh, M. Juelsholt, K. M. Ø. Jensen, K. Anklam, H. Wan, J. Schäfer, K. Čépe, M. Escudero-Escribano, J. Rossmeisl, A. Quade, V. Brüser and M. Arenz, Self-supported Pt-CoO networks combining high specific activity with high surface area for oxygen reduction, *Nat. Mater.*, 2021, **20**(2), 208–213, DOI: 10.1038/s41563-020-0775-8.

30 A. W. Jensen, G. W. Sievers, K. D. Jensen, J. Quinson, J. A. Arminio-Ravelo, V. Brüser, M. Arenz and M. Escudero-Escribano, Self-supported nanostructured iridium-based networks as highly active electrocatalysts for oxygen evolution in acidic media, *J. Mater. Chem. A*, 2020, **8**(3), 1066–1071, DOI: 10.1039/C9TA12796H.

31 C. Schneemann, J. Traegner, L. Mindermann, M. Friedrichs-Schucht, B. Tang, A. Dietzel, J. Koehler and M. Oezaslan, A Universal Analytical Model for the Limiting Current Characteristics in Impinging Jet Electrodes, *J. Electrochem. Soc.*, 2025, **172**, 66503, DOI: 10.1149/1945-7111/add840.

32 T. Biegler, D. Rand and R. Woods, Limiting oxygen coverage on platinized platinum; Relevance to determination of real platinum area by hydrogen adsorption, *J. Electroanal. Chem. Interfacial Electrochem.*, 1971, **29**(2), 269–277, DOI: 10.1016/S0022-0728(71)80089-X.

33 R. Woods, Hydrogen adsorption on platinum, iridium and rhodium electrodes at reduced temperatures and the determination of real surface area, *J. Electroanal. Chem. Interfacial Electrochem.*, 1974, **49**(2), 217–226, DOI: 10.1016/S0022-0728(74)80229-9.

34 F. Neese, The ORCA program system, *Wiley Interdiscip. Rev.: Comput. Mol. Sci.*, 2012, **2**(1), 73–78, DOI: 10.1002/wcms.81.

35 A. D. Becke, Density-functional exchange-energy approximation with correct asymptotic behavior, *Phys. Rev. A*, 1988, **38**(6), 3098–3100, DOI: 10.1103/PhysRevA.38.3098.

36 S. M. Tekarli, M. L. Drummond, T. G. Williams, T. R. Cundari and A. K. Wilson, Performance of density functional theory for 3d transition metal-containing complexes: utilization of the correlation consistent basis sets, *J. Phys. Chem. A*, 2009, **113**(30), 8607–8614, DOI: 10.1021/jp811503v.

37 E. van Lenthe, J. G. Snijders and E. J. Baerends, The zero-order regular approximation for relativistic effects: The effect of spin–orbit coupling in closed shell molecules, *J. Chem. Phys.*, 1996, **105**(15), 6505–6516, DOI: 10.1063/1.472460.

38 S. Grimme, S. Ehrlich and L. Goerigk, Effect of the damping function in dispersion corrected density functional theory, *J. Comput. Chem.*, 2011, **32**(7), 1456–1465, DOI: 10.1002/jcc.217591.

39 C. Powell, *X-Ray Photoelectron Spectroscopy Database XPS,Version 4.1, NIST Standard Reference Database 20*, accessed 2023-11-30.

40 L. Li, H. Liu, C. Qin, Z. Liang, A. Scida, S. Yue, X. Tong, R. R. Adzic and S. S. Wong, Ultrathin Pt x Sn 1− x Nanowires for Methanol and Ethanol Oxidation Reactions: Tuning Performance by Varying Chemical Composition, *ACS Appl. Nano Mater.*, 2018, **1**(3), 1104–1115, DOI: 10.1021/acsanm.7b00289.

41 L. Da Silva, V. Alves, S. de Castro and J. Boodts, XPS study of the state of iridium, platinum, titanium and oxygen in thermally formed IrO_2+TiO_2+PtO_X films, *Colloids Surf., A*, 2000, **170**(2–3), 119–126, DOI: 10.1016/S0927-7757(99)00535-X.

42 K. P. A. Kepp, Quantitative Scale of Oxophilicity and Thiophilicity, *Inorg. Chem.*, 2016, **55**(18), 9461–9470, DOI: 10.1021/acs.inorgchem.6b01702.

43 F. Bizzotto, J. Quinson, A. Zana, J. J. K. Kirkensgaard, A. Dworzak, M. Oezaslan and M. Arenz, Ir nanoparticles with ultrahigh dispersion as oxygen evolution reaction (OER) catalysts: synthesis and activity benchmarking, *Catal. Sci. Technol.*, 2019, **9**(22), 6345–6356, DOI: 10.1039/C9CY01728C.

44 Q.-S. Chen, J. Solla-Gullón, S.-G. Sun and J. M. Feliu, The potential of zero total charge of Pt nanoparticles and polycrystalline electrodes with different surface structure: The role of anion adsorption in fundamental electrocatalysis, *Electrochim. Acta*, 2010, **55**(27), 7982–7994, DOI: 10.1016/j.electacta.2010.03.050.

45 T. Reier, M. Oezaslan and P. Strasser, Electrocatalytic Oxygen Evolution Reaction (OER) on Ru, Ir, and Pt Catalysts: A Comparative Study of Nanoparticles and Bulk Materials, *ACS Catal.*, 2012, **2**(8), 1765–1772, DOI: 10.1021/cs3003098.

46 P. Liao, C. Chen, W. Ho, Y. Huang and K. Tiong, Characterization of IrO2 thin films by Raman spectroscopy, *Thin Solid Films*, 1997, **301**(1–2), 7–11, DOI: 10.1016/S0040-6090(96)09545-4.

47 Y. S. Huang, S. S. Lin, C. R. Huang, M. C. Lee, T. E. Dann and F. Z. Chien, Raman spectrum of IrO2, *Solid State Commun.*, 1989, **70**(5), 517–522, DOI: 10.1016/0038-1098(89)90942-3.

48 G. W. Graham, W. H. Weber, J. R. McBride and C. R. Peters, Raman investigation of simple and complex oxides of platinum, *J. Raman Spectrosc.*, 1991, **22**(1), 1–9, DOI: 10.1002/jrs.1250220102.

49 J.-C. Dong, M. Su, V. Briega-Martos, L. Li, J.-B. Le, P. Radjenovic, X.-S. Zhou, J. M. Feliu, Z.-Q. Tian and J.-F. Li, Direct In Situ Raman Spectroscopic Evidence of Oxygen Reduction Reaction Intermediates at High-Index Pt(*hkl*) Surfaces, *J. Am. Chem. Soc.*, 2020, **142**(2), 715–719, DOI: 10.1021/jacs.9b12803.

50 J.-C. Dong, X.-G. Zhang, V. Briega-Martos, X. Jin, J. Yang, S. Chen, Z.-L. Yang, D.-Y. Wu, J. M. Feliu, C. T. Williams, Z.-Q. Tian and J.-F. Li, In situ Raman spectroscopic evidence for oxygen reduction reaction intermediates at platinum single-crystal surfaces, *Nat. Energy*, 2019, **4**(1), 60–67, DOI: 10.1038/s41560-018-0292-z.

51 L. Moriau, M. A. Nazrulla, A. Logar, L. Pavko, M. Bele, N. Hodnik and A. K. Surca, Ir metal nanoparticles and IrO2 for acidic oxygen evolution reaction: Insight from Raman spectroscopy, *Sustainable Mater. Technol.*, 2024, **40**, e00901, DOI: 10.1016/j.susmat.2024.e00901.

52 S. Zou, H. Y. H. Chan, C. T. Williams and M. J. Weaver, Formation and Stability of Oxide Films on Platinum-Group Metals in Electrochemical and Related Environments As Probed by Surface-Enhanced Raman Spectroscopy: Dependence on the Chemical Oxidant, *Langmuir*, 2000, **16**(2), 754–763, DOI: 10.1021/la990544i.

53 Y. Mo, I. C. Stefan, W.-B. Cai, J. Dong, P. Carey and D. A. Scherson, In Situ Iridium L III -Edge X-ray Absorption and Surface Enhanced Raman Spectroscopy of Electrodeposited Iridium Oxide Films in Aqueous Electrolytes, *J. Phys. Chem. B*, 2002, **106**(14), 3681–3686, DOI: 10.1021/jp014452p.

54 M. van der Merwe, R. E. Wibowo, C. E. Jimenez, C. Escudero, G. Agostini, M. Bär and R. Garcia-Diez, Electronic and Structural Property Comparison of Iridium-Based OER Nanocatalysts Enabled by Operando Ir L 3 -Edge X-ray Absorption Spectroscopy, *ACS Catal.*, 2024, **14**(22), 16759–16769, DOI: 10.1021/acscatal.4c03562.

55 Y.-H. Wang, J.-B. Le, W.-Q. Li, J. Wei, P. M. Radjenovic, H. Zhang, X.-S. Zhou, J. Cheng, Z.-Q. Tian and J.-F. Li, In situ Spectroscopic Insight into the Origin of the Enhanced Performance of Bimetallic Nanocatalysts towards the Oxygen Reduction Reaction (ORR), *Angew. Chem., Int. Ed.*, 2019, **58**(45), 16062–16066, DOI: 10.1002/anie.201908907.

56 I. Katsounaros, W. B. Schneider, J. C. Meier, U. Benedikt, P. U. Biedermann, A. A. Auer and K. J. J. Mayrhofer, Hydrogen peroxide electrochemistry on platinum: towards understanding the oxygen reduction reaction mechanism, *Phys. Chem. Chem. Phys.*, 2012, **14**(20), 7384–7391, DOI: 10.1039/C2CP40616K.

57 A. M. Gómez-Marín and E. A. Ticianelli, A reviewed vision of the oxygen reduction reaction mechanism on Pt-based catalysts, *Curr. Opin. Electrochem.*, 2018, **9**, 129–136, DOI: 10.1016/j.coelec.2018.03.008.

58 B. A. Sexton, Vibrational spectra of water chemisorbed on platinum (111), *Surf. Sci.*, 1980, **94**(2–3), 435–445, DOI: 10.1016/0039-6028(80)90017-5.

59 Y. Zhang, X. Gao and M. J. Weaver, Nature of surface bonding on voltammetrically oxidized noble metals in aqueous media as probed by real-time surface-enhanced Raman spectroscopy, *J. Phys. Chem.*, 1993, **97**(33), 8656–8663, DOI: 10.1021/j100135a020.

60 H. Y. H. Chan, S. Zou and M. J. Weaver, Mechanistic Differences between Electrochemical and Gas-Phase Thermal Oxidation of Platinum-Group Transition Metals As Discerned by Surface-Enhanced Raman Spectroscopy, *J. Phys. Chem. B*, 1999, **103**(50), 11141–11151, DOI: 10.1021/jp992500o.

61 F. Sugimura, N. Sakai, T. Nakamura, M. Nakamura, K. Ikeda, T. Sakai and N. Hoshi, In situ observation of Pt oxides on the low index planes of Pt using surface enhanced Raman spectroscopy, *Phys. Chem. Chem. Phys.*, 2017, **19**(40), 27570–27579, DOI: 10.1039/C7CP04277A.

62 P. Sabatier La catalyse en chimie organique. *Encyclopédie de Science Chimique Appliquée,* Dunham, 1913.

63 H. Y. Lim, S. O. Park, S. H. Kim, G. Y. Jung and S. K. Kwak, First-Principles Design of Rutile Oxide Heterostructures for Oxygen Evolution Reactions, *Front. Energy Res.*, 2021, **9**, 606313, DOI: 10.3389/fenrg.2021.606313.

64 Z. W. Seh, J. Kibsgaard, C. F. Dickens, I. Chorkendorff, J. K. Nørskov and T. F. Jaramillo, Combining theory and experiment in electrocatalysis: Insights into materials design, *Science*, 2017, **355**(eaad4998), DOI: 10.1126/science.aad4998.

65 D. F. Abbott, D. Lebedev, K. Waltar, M. Povia, M. Nachtegaal, E. Fabbri, C. Copéret and T. J. Schmidt, Iridium Oxide for the Oxygen Evolution Reaction: Correlation between Particle Size, Morphology, and the Surface Hydroxo Layer from Operando XAS, *Chem. Mater.*, 2016, **28**(18), 6591–6604, DOI: 10.1021/acs.chemmater.6b02625.

66 A. Minguzzi, O. Lugaresi, E. Achilli, C. Locatelli, A. Vertova, P. Ghigna and S. Rondinini, Observing the oxidation state turnover in heterogeneous iridium-based water oxidation catalysts, *Chem. Sci.*, 2014, **5**(9), 3591, DOI: 10.1039/C4SC00975D.

67 A. Minguzzi, C. Locatelli, O. Lugaresi, E. Achilli, G. Cappelletti, M. Scavini, M. Coduri, P. Masala, B. Sacchi, A. Vertova, P. Ghigna and S. Rondinini, Easy Accommodation of Different Oxidation States in Iridium Oxide Nanoparticles with Different Hydration Degree as Water Oxidation Electrocatalysts, *ACS Catal.*, 2015, **5**(9), 5104–5115, DOI: 10.1021/acscatal.5b01281.

68 M. van der Merwe, Y. Lee, R. E. Wibowo, T. Kokumai, A. Efimenko, M. D. Arce, C. E. Jimenez, B. Howchen, R. Suarez Anzorena, I. Lucentini, C. Escudero, G. Schuck, Z. Kochovski, M. Favaro, D. E. Starr, K. Reuter, C. Scheurer, M. Bär and R. Garcia-Diez, Unravelling the mechanistic complexity of the oxygen evolution reaction and Ir dissolution in highly dimensional amorphous hydrous iridium oxides, *Energy Environ. Sci.*, 2025, **18**(3), 1214–1231, DOI: 10.1039/D4EE02839B.